Night Vision and Electronic Sensors Directorate

AMSRD-CER-NV-TR-245

Background Modeling and Algorithm Fusion For Airborne Landmine Detection

December 2005

Approved for public release; Distribution unlimited

Fort Belvoir, Virginia 22060-5806

REPORT DOCUMENTATION PAGE

Form Approved
OMB No. 0704-0188

1. AGENCY USE ONLY *(Leave blank)*	2. REPORT DATE	3. REPORT TYPE AND DATES COVERED
	December 2005	Final Thesis - 2004

4. TITLE AND SUBTITLE
Background Modeling and Algorithm Fusion For Airborne Landmine Detection

5. FUNDING NUMBERS
DAAB07-01-D-G601/
W15P7T-05-R-B497

6. AUTHOR(S)
Hariharan Ramachandran

7. PERFORMING ORGANIZATION NAME(S) AND ADDRESS(ES)
University of Missouri-Rolla
Graduate School of Electrical Engineering

8. PERFORMING ORGANIZATION REPORT NUMBER

9. SPONSORING / MONITORING AGENCY NAME(S) AND ADDRESS(ES)
Night Vision and Electronic Sensors Directorate
Countermine Division (Anh Trang)
10221 Burbeck Road
Fort Belvoir, VA 22060-5806

10. SPONSORING / MONITORING AGENCY REPORT NUMBER
AMSRD-CER-NV-TR-245

11. SUPPLEMENTARY NOTES

12a. DISTRIBUTION / AVAILABILITY STATEMENT
Approve for Public Release; Distribution Unlimited

12b. DISTRIBUTION CODE
A

13. ABSTRACT *(Maximum 200 words)*

Airborne mine and minefield detection has been an active topic of research in recent times. The detection process looks for local anomalies in the acquired mid-wave infrared imagery. An anomaly is any mine size image feature that is different from its immediate surrounds. The so called RX algorithm by Reed and Yu has been used extensively in airborne mine detection systems as the anomaly detector. The RX detector measures the local signal to clutter ratio assuming a zero mean uncorrelated Gaussian background. The airborne minefield detection system is expected to detect possible mines and minefields over various types of terrains, different soil conditions and at different times of the day. For most terrains conditions, the background is often correlated and inhomogeneous. This raises the question as to whether the performance can be made invariant to terrain characteristics. The primary aim behind this thesis is to model the distributions for RX statistics of false alarms under more realistic background conditions. This modeling is expected to facilitate the study of the detectability of mines and minefields in various backgrounds. By modeling various backgrounds, guidelines can be obtained for likely false alarms rates for different backgrounds. Algorithmic fusion is simple but often effective tool to derive optimum performance from multiple detection algorithms. The parameters obtained from background modeling can be use as a catalyst for algorithm fusion and thereby improve detection performance for a given set of detector algorithms.

14. SUBJECT TERMS
Landmine Detection, Ground-based mine detection, Airborne minefield detection, AMIDARS, REMIDS, ASTAMIDS, COBRA, AIRMS, AFIRMIS, LAMD, Algorithmic Fusion, Decision level fusion, Mine Signature, Detection architecture, RX anomaly detector

15. NUMBER OF PAGES
102

16. PRICE CODE

17. SECURITY CLASSIFICATION OF REPORT	18. SECURITY CLASSIFICATION OF THIS PAGE	19. SECURITY CLASSIFICATION OF ABSTRACT	20. LIMITATION OF ABSTRACT
UNCLASSIFIED	UNCLASSIFIED	UNCLASSIFIED	None

BACKGROUND MODELING AND ALGORITHM FUSION FOR AIRBORNE LANDMINE DETECTION

by

HARIHARAN RAMACHANDRAN

A THESIS

Presented to the Faculty of the Graduate School of the

UNIVERSITY OF MISSOURI-ROLLA

In Partial Fulfillment of the Requirements for the Degree

MASTER OF SCIENCE IN ELECTRICAL ENGINEERING

2004

Approved by

Sanjeev Agarwal, Advisor

O. Robert Mitchell

R. Joe Stanley

ABSTRACT

Airborne mine and minefield detection has been an active topic of research in recent times. The detection process looks for local anomalies in the acquired mid-wave infrared imagery. An anomaly is any mine size image feature that is different from its immediate surrounds. The so called RX algorithm by Reed and Yu [22] has been used extensively in airborne mine detection systems as the anomaly detector. The RX detector measures the local signal to clutter ratio assuming a zero mean uncorrelated Gaussian background. The airborne minefield detection system is expected to detect possible mines and minefields over various types of terrains, different soil conditions and at different times of the day. For most terrain conditions, the background is often correlated and inhomogeneous. This raises the question as to what kind of detection performance can be achieved for different terrains and whether the performance can be made invariant to terrain characteristics.

The primary aim behind this thesis is to model the distributions for RX statistics of false alarms under more realistic background conditions. This modeling is expected to facilitate the study of the detectability of mines and minefields in various backgrounds. By modeling various backgrounds, guidelines can be obtained for likely false alarm rates for different backgrounds. Algorithmic fusion is a simple but often effective tool to derive optimum performance from multiple detection algorithms. The parameters obtained from background modeling can be used as a catalyst for algorithm fusion and thereby improve detection performance for a given set of detector algorithms.

ACKNOWLEDGMENTS

I am highly grateful to my advisor, Dr. Sanjeev Agarwal, for his constant encouragement and support throughout my Masters program. Without his support, this work would not have been possible. My gratitude is also extended towards Dr. Robert Mitchell for agreeing to be on my committee and provide some important tips during the brief meetings I have had with him during my graduate program. I would like to thank Dr. Stanley for being one of my committee members. I would also like to thank the students of my research group especially Thandava, Deepak Menon and Ritesh for their help in making this thesis a reality.

I would also like to thank the Countermine Division of Night Vision and Electronic Sensors Directorate (NVESD) for providing the data and the opportunity to work on this project. Last, but definitely not the least, I would like to express eternal gratitude towards my family for being there for me whenever it mattered the most.

TABLE OF CONTENTS

Page

LIST OF ILLUSTRATIONS

Figure Page

LIST OF TABLES

Table Page

1. INTRODUCTION

Landmine detection has been a topic of significant research interest in recent times. The primary focus of research has been to find a time-effective, feasible and trustworthy solution to anti-personnel and anti-tank mine detection and demining. The motivation behind this step towards mine detection research is to facilitate cost-effective humanitarian demining as well as to gain a significant advantage in tactical offense and defense capabilities. The US Army has been experimenting with a wide variety of technologies to come up with a safe and reliable solution to the problem of landmine detection. The emphasis of this thesis is on research conducted with airborne landmine detection which is applicable primarily to a tactical warfare scenario.

1.1. TYPES OF LANDMINE DETECTION

All mine detection technologies can be classified into two major categories:

- Ground-based mine detection
- Airborne minefield detection

The basics of each of these detection schemes can be elucidated in the following sections.

1.1.1. Ground Based Mine Detection. Handheld and vehicular mine detection are the two ground-based mine detection schemes. They primarily consist of a human carrying a mine detection device or a vehicle mounted with the same, scanning the immediate neighborhood for mines. The standoff distance of the handheld detector determines the extent of the immediate neighborhood investigated by the sensor. Whereas, handheld detection cannot essentially neutralize the mine, some vehicular detection systems come with such features. One major disadvantage of the handheld system is the potential danger that it poses to the human operator. Also, vehicular systems are faster in scanning a particular area compared to the human operating the handheld device. Some of the technologies currently employed or being explored for handheld detection are:

1. Electromagnetic Induction (Metal Detector) [1]
2. Ground Penetrating Radar (GPR) [2]
3. Electromagnetic Induction Spectroscopy (EMIS) [3]

4. Neutron Backscattering [4]
5. Nuclear Quadruple Resonance (NQR) [5]
6. Water Jet Demining [6]

Vehicle based landmine detection has the advantage that a human is not directly involved. Vehicular demining systems can also be equipped with multiple sensors which can help improve reliability of detection and in the demining of a variety of mine types like plastic and metallic mines. Some of the vehicular demining systems in existence or under research include:

1. Swarm intelligence based vehicular detection [7]
2. Robotic Landmine Search [8]
3. Vehicular Mine Detection Test bed (VMDT) [9]
4. Waterjet based landmine destroyer (ELADIN) [10]

1.1.2. Airborne Landmine Detection. The mine detection method explained above is not automatic. Handheld and vehicular systems basically operate on the following paradigms [11]:

- Handheld: swing, detect, localize, stop and mark.
- Vehicular: move forward, detect mark and stop/overpass/neutralize.

Both these methods have limited standoff distance. Because of this, airborne landmine detection has been gaining a lot of importance. Recent emphasis on highly mobile force capabilities has further given currency to airborne landmine detection. A number of programs and schemes are being devised to come up with a feasible solution. The time involved in scanning a huge area is minimal compared to ground based detection. The collection of data from a large area mandates the development of automatic / aided target recognition (ATR/AiTR) systems. While many of the ground based detection schemes operate on electromagnetic, radio and acoustic signals, most airborne landmine detection systems under research, employ active or passive electro-optical imagery.

Sensors that are built for airborne landmine detection are primarily imaging sensors that operate over various frequency bands in the EM spectrum. Many sensors operate in the mid-wave infra red (MWIR) frequency range as this frequency band is

sensitive to the thermal contrast and has desirable spatial resolution. Significant thermal contrast can be found between metallic and non-metallic mines and typical backgrounds for surface as well as buried mines, making the imaging more convenient than other systems. Some other types of airborne sensors under research for landmine detection are Laser based sensors (active electro – optical) [12] and Radar based sensors [13]. Imaging for most of the airborne detection schemes is done using low altitude aircraft equipped with camera sensors. Some of the different camera sensors used in airborne landmine detection are based on the following imaging technologies:

- Mid-Wave Infra Red sensor [14]
- Hyper-spectral imaging sensor [15]
- Active Laser (~808nm range) [12]
- Multi-band Infra Red sensor [16]

1.2. SENSOR TECHNOLOGIES AND ALGORITHMS USED IN AIRBORNE LANDMINE DETECTION

Some of the programs currently engaged in the development of airborne landmine detection system, are: Airborne Minefield Detection and Reconnaissance System (AMIDARS) [17], Remote Minefield Detection System (REMIDS) [18], Airborne Standoff Minefield Detection System (ASTAMIDS) [17], Coastal Battlefield Reconnaissance and Analysis System (COBRA) [16], Airborne Infrared Measurement System (AIRMS) [19], Airborne Far IR Minefield Imaging System (AFIRMIS) [20], and the Lightweight Airborne Multi-spectral Minefield Detection System (LAMD) [14]. Important features of these programs pertaining to the sensor technologies and algorithms used are reviewed in the following.

AMIDARS [17] consists of a thermal line scan sensor (in the mid IR region) and a ground based processing environment. The sensor is flown on an aircraft acting as a substitute for an Unmanned Aerial Vehicle (UAV). The sensor is designed primarily to be deployed on a UAV. The imagery from the sensor is recorded with the help of a digital recorder and the ground facility processes the recorded data after the flight mission is concluded.

The REMIDS [18] program was primarily meant to discover and clear Unexploded Ordnance (UXO) that fills up a huge amount of government owned land. The primary purpose of this exercise was to clear away the UXOs to make use of the land recovered for purposes other than that of military nature. REMIDS uses an airborne line scanner with sensors to measure the reflectance, polarization and the thermal characteristics. The sensors for reflectance and polarization are active sensors and the one for thermal response is a passive sensor. The three channels in the imagery are optically co-registered and are in the thermal IR and near IR spectral bands. In the case of this program, the digitized data that is obtained from the sensors is analyzed first by a computer, which classifies each pixel of the image to be a contribution of the UXO or the background. The second stage of processing basically imposes size criteria on the images clearing away misfits. The last stage of the whole operation includes an operator manually classifying the objects to be UXOs or otherwise.

ASTAMIDS [17] can be considered as the evolution of the AMIDARS and the REMIDS programs. This particular program makes use of infrared imagery as well. It takes two parallel paths towards airborne landmine detection. The first approach makes use of a combination of active and passive infra-red sensors for imagery and the second approach makes use of a passive infra-red sensor alone. In terms of concept, the ASTAMIDS system closely resembles the AMIDARS system and more appropriately forms the demonstration and validation part of AMIDARS and REMIDS.

The COBRA system [16] includes an airborne passive multi-spectral imaging subsystem for data collection and a ground station for real-time system tracking and post-mission processing. The imaging subsystem consists of a multi-spectral intensified video camera with a spinning filter wheel. The sensor under question operates in the 400 to 900 nm range of the EM spectrum and it makes use of primarily 6 different spectral bands in the above wavelength range. The ground station subsystem of the COBRA program is called the COBRA Tactical Information Display System (CTIDS). The CTIDS is further organized into a Real-time function (RTF) subsystem and the post-mission processing (PMP) subsystem. The RTF subsystem allows the CTIDS to record the multispectral imagery with the help of a real-time video downlink, digitize the received imagery and also archive the imagery along with other required information. The PMP subsystem

provides the CTIDS automated minefield detection procedures using the COBRA sensory imagery. The detection algorithm that COBRA uses is primarily a modification of the Reed-Xiaoli (RX) anomaly detection algorithm as published by Holmes et al. [21]. Once potential mine locations have been obtained, separate algorithms are used for patterned and scattered minefield detection.

AIRMS [19] is another program that uses infra-red imagery. This program operates by applying matched filter processing and multi-frame integration on infrared detection of moving targets in background clutter. The imagery is obtained in the 8.2 – 12.2 μ m long wave range. The AIRMS sensor consists of a 24 inch aperture infrared telescope along with supporting components. It is a scanning type system in which the detector elements are integrated together with the help of a time-delay integrate (TDI) circuit.

AFIRMIS [20] or the Airborne Far Infra-Red Imaging System is a combination of a passive and an active system which performs the fusion of information from the emissivity, the reflectivity and the three dimensional profile of the target / background scene in order to improve the probability of detection and also reduce the false-alarm rate. The imaging that is used in this scheme is of the passive long wave infrared (LWIR) type.

The LAMD [14] system makes use of an Electro-Optical/Infra-Red (EO/IR) sensor and the imagery data collected is usually in the Mid Wave Infra Red (MWIR) region of the EM spectrum. Multiple channels or bands of the data are collected with the help of appropriate filters similar to the filter system used in the COBRA program. The LAMD program is still in the development stage with multiple detection and discrimination algorithms being put forward by different research groups. The Reed-Xiaoli algorithm is the prime contender for implementation as the anomaly detector. This program also backs research on false alarm mitigation and minefield detection as the final goal of any of these systems is to detect minefields and not just mines.

1.3. BACKGROUND MODELING AND ALGORITHMIC FUSION

The latest development in the current program has been the collection of imagery data over a variety of backgrounds with and without mine targets. The primary purpose

behind this kind of data collection is to allow for in-depth background analysis which should give a measure of the effect of the background on the detection and discrimination of mines and minefields. This line of thought forms the primary motivation behind image background modeling and algorithmic fusion which is the topic of this thesis. Image background modeling provides a better understanding of the whole detection process, in that, it can be used to statistically differentiate between different backgrounds and also explain the performance of the anomaly detector and the whole detection system under these background conditions. Another application of background modeling is to study the compatibility of mines in various backgrounds. To be more meaningful, by modeling various backgrounds, guidelines can be set as to what kind of mines would be detectable / not detectable in each of the different backgrounds.

Algorithmic fusion is a simple but effective tool to derive optimum performance from multiple detection algorithms. The motivation behind doing algorithmic fusion in this work is to build an anomaly detector that gives the maximum detection output irrespective of the algorithms or the parameters of the algorithms under evaluation. In this particular work, algorithmic fusion for different size of targets for the RX algorithm is evaluated.

1.4. OVERVIEW OF THE THESIS

The thesis consists of six sections. Section 2 gives a brief description of the data used in the thesis along with a preliminary analysis of the data that gives a statistical overview of the available imagery data. Section 3 presents a detailed explanation of the RX anomaly detector and the detection architecture used for the work presented here. Section 3 also provides the development of the statistical model for detection statistics.

Section 4 begins with motivation for background modeling and its advantages. Statistical modeling of detection statistics for different types of background terrain is discussed. Some results of such modeling for simulated data and for background only data are presented.

Section 5 provides the necessary background theory and development of the algorithmic fusion scheme implemented here. The detailed results obtained for each

dataset and possible combinations of outputs generated are displayed and the results discussed in this section.

Section 6 gives a detailed summary of all the previous sections and gives the reader a modicum of insight into the improvements that can be done in the future and also other possible implementations of the algorithms discussed in this thesis.

Appendix A explains the LAMDFAM GUI, which has been pivotal in generating the results reported here. A brief summary of the GUI is presented. This section also provides the merits and demerits of using such visualization and processing aids.

Appendix B gives a listing of important program code used to implement the ideas and concepts discussed in this thesis. The function prototypes used with detailed explanation of the variables used in MATLAB are discussed, along with the utility of these functions.

2. DATA DESCRIPTION AND PRELIMINARY ANALYSES

Over the last two years, significant amount of real airborne data has been collected as part of the development exercise for the airborne landmine detection program at NVESD. The imagery is collected by a low flying (1500 ft.) aircraft over different terrain during four different times of the day with narrow field of view and a GSD of approximately 1.1 inch. Each flight of data collection is called a run which consists of a certain number of images (called frames) captured at approximately 8 frames per second. Each image is of dimension 512 x 640. The data is collected for different mid wave infra red (MWIR) bands. The four different times of the day span the whole 24 hours and so there are both day and nighttime images. The images that are collected during the daytime have the hint of shadows next to the mines thus providing a challenge to the anomaly detector and also the algorithms that follow. The nighttime images have the heat signature of the mines and this varies as per the composition of the mines and the background vegetation. Some of the common features of the airborne imagery data that spans across all the data collections are listed below:

- Mines Types: Different types of mines can be classified based on size (large, medium, small), composition (metal, plastic) or method of placement (surface, buried):
    - Large surface mines : LP_B (plastic) and LM_A (metal)
    - Medium surface mines : MP_A (plastic)
    - Small surface mines : SM_A (metal)
    - Large Buried mines : LM_A_B (large metal), LM_C_B (large metal) and LP_D_B (large plastic).
    - Medium Buried mine : MP_A_B (medium plastic)
- The four spectral bands in the MWIR spectrum range for which the data is collected are identified as:
    - Full band (3 – 5 μm) – Band 0, Band 1
    - Solar band (3 – 4 μm) – Band 2

- Thermal band 1 (4 – 4.5 μm) – Band 3
- Thermal band 2 (4.5 – 5 μm) – Band 4

The specifics of data collected during May 2002, August 2002, October 2002 and May 2003 along with tables listing detailed statistics of each of the collections are presented in the next few sections.

2.1. MAY 2002 DATA

The data collected during May 2002 consists of 13 different runs with 143 frames each covering a terrain that was made up of both vegetation and specifically prepared lanes with different background types. The mines were primarily laid in the prepared lanes. The lanes represent different soil types such as short grass, tall grass, sand and clay. Each lane contains few different types of mines in a patterned manner. There are patterned mines in normal soil as well, outside the lane area. The general trend found in the 13 datasets at hand is that, the first few frames and last few are composed of heavy vegetation. The frames in the middle of the run are typically the ones over lane areas and these frames contain the minefields.

Table 2.1 gives various numbers of mines found in different runs for this dataset categorized according to band, time of day, and surface laid or buried. The total number of buried and surface mines is also presented for each band and each time of day. Table 2.2 gives the number of frames with mines, and number of different types of mines found in the dataset. This comparison of file numbers can be used to observe the distribution of mines present in the data and also to give a measure of similarity of mine distribution over different bands. Along with these numbers, the ratio of the total number of surface mines to the total number of buried mines present is also given for each band and time of day. From the table, it is seen that the number of buried mines is lesser compared to the number of surface mines. Also, the number of frames that carry mines is small as compared to total number of available frames. It is noted from Table 2.1 and 2.2 that except for Band 1, all the other three bands do not have data in the 3:00 – 4:30 and 22:00 – 23:00 time periods. There are no buried mines in the runs coming under Band 2 – 9:00 – 11:00 and Band 4 – 18:00 – 19:00.

Table 2.1. Distribution of Available May 2002 Data by Mine Type.

		Surface Mines					Buried Mines			All Mines
Bands	Times	LM_A	LP_B	MP_A	SM_A	TOTAL	MP_A_B	LM_A_B	TOTAL	TOTAL
Band - 1 (full)	3:00 - 4:30	25	22	25	0	72	25	19	44	116
	9:00 - 11:00	17	15	7	4	43	16	15	31	74
	18:00 - 19:00	30	8	19	26	83	2	4	6	89
	22:00 - 23:00	25	10	12	7	54	11	9	20	74
Band - 2 (solar)	3:00 - 4:30	-	-	-	-	-	-	-	-	-
	9:00 - 11:00	26	0	31	0	57	0	0	0	57
	18:00 - 19:00	29	4	0	3	36	15	13	28	64
	22:00 - 23:00	-	-	-	-	-	-	-	-	-
Band - 3 (thermal 1)	3:00 - 4:30	-	-	-	-	-	-	-	-	-
	9:00 - 11:00	24	18	7	18	67	9	9	18	85
	18:00 - 19:00	53	20	3	25	101	12	13	25	126
	22:00 - 23:00	-	-	-	-	-	-	-	-	-
Band - 4 (thermal 2)	3:00 - 4:30	-	-	-	-	-	-	-	-	-
	9:00 - 11:00	46	31	12	30	119	14	14	28	147
	18:00 - 19:00	26	0	16	24	66	0	0	0	66
	22:00 - 23:00	-	-	-	-	-	-	-	-	-

Table 2.2. Distribution of Available May 2002 Data by Image Frames.

		3:00 - 4:30	9:00 - 11:00	18:00 - 19:00	22:00 - 23:00
Band - 1 (full)	No. of Frames	286	143	143	143
	Frames with Mines	21	10	9	10
	Mines (Surface/Buried)	72 / 44	43/ 31	83 / 6	24/ 20
Band - 2 (solar)	No. of Frames	-	143	143	-
	Frames with Mines	-	10	7	-
	Mines (Surface/Buried)	-	57 / 0	36 / 28	-
Band - 3 (thermal 1)	No. of Frames	-	143	286	-
	Frames with Mines	-	11	17	-
	Mines (Surface/Buried)	-	67 / 18	74 / 25	-
Band - 4 (thermal 2)	No. of Frames	-	286	143	-
	Frames with Mines	-	17	8	-
	Mines (Surface/Buried)	-	119/ 28	66 / 0	-

2.2. AUGUST 2002 DATA

The August 2002 data consisted of a smaller set of data, about 9 runs of 143 files each and 1 run with 142 files collected at the same site as the May 2002 data. The data consists only of collections in two spectral bands, Bands 0 and 1 in the MWIR region of 3.4 μm – 5.1 μm. This is a considerably abbreviated collection of data. A mixture of buried and surface mines of the types mentioned in Section 2.1 is present in this data as well. Table 2.3 shows the distribution of different mine types for each band and different times of the day.

Table 2.3. Distribution of Available August 2002 Data by Mine Type.

		Surface Mines					Buried Mines		All Mines
Bands	Times	LM_A	LP_B	MP_A	SM_A	TOTAL	MP_A_B	TOTAL	TOTAL
Band - 0 (full)	0:00 - 1:30	85	27	31	54	197	27	27	224
	3:00 - 4:30	-	-	-	-	-	-	-	-
	8:00 - 9:30	-	-	-	-	-	-	-	-
	18:00 - 19:30	94	31	30	68	223	30	30	253
Band - 1 (full)	0:00 - 1:30	-	-	-	-	-	-	-	-
	3:00 - 4:30	47	20	16	37	120	20	20	140
	8:00 - 9:30	50	15	20	34	119	15	15	134
	18:00 - 19:30	-	-	-	-	-	-	-	-

Table 2.4 shows the distribution of data in terms of frames, viz., number of frames present in each band for each time of day and the number of frames which have mines and the ratio of surface mines to buried mines. Here, buried mines are comparatively less in number to the surface mines. As can be seen from Table 2.4, Band 0 has data only in two time periods namely, 0:00 – 1:30 and 18:00 – 19:30 and Band 1 has data only in two other time periods namely, 3:00 – 4:30 and 8:00 – 9:30. But one observation that can be made out of this is that, there is an even distribution of both nighttime and daytime runs in both Bands 0 and 1. There are more runs collected in Band 0 than in Band 1. But the number of frames that contain mines in each run is almost constant; and in most cases the frames containing mines follow sequentially.

Table 2.4. Distribution of Available August 2002 Data by Image Frames.

		0:00 - 1:30	3:00 - 4:30	8:00 - 9:30	18:00 - 19:30
Band - 0 (full)	No. of Frames	428	-	-	429
	Frames with Mines	34	-	-	35
	Mines (Surface/Buried)	197 / 27	-	-	223 / 30
Band - 1 (full)	No. of Frames	-	286	286	-
	Frames with Mines	-	25	19	-
	Mines (Surface/Buried)	-	120 / 20	119 / 15	-

2.3. OCTOBER 2002 DATA

The WESCAM October 2002 data consists of 15 runs. The 15 runs contain data from three missions over different times of the day and bands. There are a total of 2143 frames (143x14 + 141x1). This particular collection of data consists of daytime data only. The primary terrain for the data collection can be classified as rocky – arid areas with light, sparse vegetation. Also, the data present contains only surface mines in it. The ground truth is available for 371 mine targets, consisting of 190 large surface mine targets (LP_B (98), LM_A (92)) and 181 small surface mine targets (SM_A (90), MP_A (91)). Ground Truth is also available for 430 fiducials. These are rejected from the false alarms at the time of analysis.

The following tables give more information regarding the data collection at hand. Table 2.5 gives the distribution of different mines over different bands and over different times of the day. It can be noted that Band 4 has data only in one time period, i.e. 10:00 – 12:00 and no data in the time period 15:00 – 17:00. There is a fairly constant density of different types of surface mines.

Table 2.6 gives the number of image frames in each band with mines along with the total number of image frames. Since the October 2002 data does not have any buried mines, mention of the same is omitted from the tables. It is apparent from this table that the number of frames with mines is about constant for all the runs.

Table 2.5. Distribution of Available October 2002 Data by Mine Type.

		Surface Mines				
Bands	Times	LM_A	LP_B	MP_A	SM_A	TOTAL
Band - 1 (full)	10:00 - 12:00	14	13	14	12	104
	15:00 - 17:00	12	15	12	12	182
Band - 2 (solar)	10:00 - 12:00	12	15	14	11	219
	15:00 - 17:00	20	19	20	20	215
Band - 3 (thermal 1)	10:00 - 12:00	12	12	11	12	136
	15:00 - 17:00	10	11	8	12	89
Band - 4 (thermal 2)	10:00 - 12:00	12	13	12	11	48
	15:00 - 17:00	-	-	-	-	-

Table 2.6. Distribution of Available October 2002 Data by Image Frames.

		10:00 - 12:00	15:00 - 17:00
Band - 1 (full)	No. of Frames	286	286
	Frames with Mines	21	17
	Mines (Surface)	53	51
Band - 2 (solar)	No. of Frames	286	429
	Frames with Mines	23	26
	Mines (Surface)	52	79
Band - 3 (thermal 1)	No. of Frames	286	286
	Frames with Mines	19	15
	Mines (Surface)	47	41
Band - 4 (thermal 2)	No. of Frames	286	-
	Frames with Mines	19	-
	Mines (Surface)	48	-

2.4. MAY 2003 DATA

The dataset for May 2003 is the biggest collection of data provided for analysis to UMR. The primary terrain with mines can be classified as arid with little or no vegetation. In this data collection, for the first time, data showing background alone has also been collected in addition to data showing both background and minefields. This has been done with the intention of doing extensive background analyses, one type of which could be similar to that done in this thesis in the following sections. The collection consists of 37765 image frames from 83 runs over mine areas from ten missions covering different times of the day and bands. It also contains 55 runs over background only areas from nine missions covering different times of day for full band (Band 0 and Band 1). The ground truth is available for 12391 mine targets of which there are 1748 large surface mine targets, 844 small surface mine targets, 3946 medium surface mine targets and 5853 buried mine targets. A detailed summary of the May 2003 data is provided in Tables 2.7 and 2.8. Table 2.7 shows number of mine signatures for each surface and buried mine of each type. Similarly for each band and each mission, Table 2.8 shows number of total frames and the number of frames with mine targets.

Table 2.7. Distribution of Available May 2003 Data by Mine Type.

		Surface Mines					Buried Mines					All Mines
Bands	Times	LM_A	LP_B	MP_A	SM_A	TOTAL	LM_A_B	LM_C_B	LP_D_B	MP_A_B	TOTAL	TOTAL
Band - 0 (full)	2:30 to 5:30	13	8	63	13	97	13	65	16	15	109	206
	16:00 to 20:00	30	27	139	27	223	28	120	24	25	197	420
	21:00 to 24:00	46	50	224	46	366	42	189	56	54	341	707
Band - 1 (full)	2:30 to 5:30	93	92	415	91	691	89	342	91	92	614	1305
	7:30 to 10:30	98	107	514	94	813	111	405	114	111	741	1554
	16:00 to 20:00	23	19	69	19	130	21	32	28	23	104	234
Band - 2 (solar)	7:30 to 10:30	109	107	500	112	828	118	414	107	109	748	1576
	16:00 to 20:00	29	32	112	26	199	25	55	19	30	129	328
Band - 3 (thermal 1)	2:30 to 5:30	86	82	379	83	630	85	293	76	82	536	1166
	7:30 to 10:30	109	112	534	109	864	121	427	119	115	782	1646
	16:00 to 20:00	31	31	86	30	178	29	101	23	27	180	358
Band - 4 (thermal 2)	2:30 to 5:30	81	83	357	75	596	75	277	68	80	500	1096
	7:30 to 10:30	99	101	479	93	772	112	357	118	109	696	1468
	16:00 to 20:00	27	23	75	26	151	29	88	30	29	176	327

Table 2.8. Distribution of Available May 2003 Data by Image Frames.

		2:30 to 5:30	7:30 to 10:30	16:00 to 20:00	21:00 to 24:00
Band - 0 (full)	No. of Frames	910	0	1365	2275
	Frames with Mines	23	0	44	74
	Mines (Surface/Buried)	97 / 109	0	223 / 197	366 / 341
Band - 1 (full)	No. of Frames	3640	4550	1365	0
	Frames with Mines	125	152	33	0
	Mines (Surface/Buried)	691 / 614	813 / 741	130 / 104	0
Band - 2 (solar)	No. of Frames	0	4550	1365	0
	Frames with Mines	0	151	38	0
	Mines (Surface/Buried)	0	828 / 748	199 / 129	0
Band - 3 (thermal 1)	No. of Frames	3185	4550	1365	0
	Frames with Mines	114	161	41	0
	Mines (Surface/Buried)	630 / 536	864 / 782	178 / 180	0
Band - 4 (thermal 2)	No. of Frames	3185	4095	1365	0
	Frames with Mines	114	142	40	0
	Mines (Surface/Buried)	596 / 500	772 / 696	151 / 176	0

Table 2.9 shows the distribution of image frames and runs for Bands 0 and 1 for the different background only data available in the May 2003 collection.

Table 2.9. Distribution of Available May 2003 Background Only Data by Image Frames.

		Number of Frames / Number of Runs					
		Yellow Sand - 2	Wash - 5	Cibola - 6	Rock - 41	Rock - 42	Rock - 44
Band - 0 (full)	2:30 - 5:30	1234 / 3	-	1300 / 2	-	-	-
	7:30 - 10:30	2449 / 6	-	2600 / 4	910 / 2	650 / 1	-
	16:00 - 20:00	817 / 2	910 / 2	1950 / 3	1365 / 3	1950 / 3	1300 / 2
	21:00 - 24:00	1228 / 3	910 / 2	1950 / 3	910 / 2	1755 / 3	1299 / 2
Band - 1 (full)	2:30 - 5:30	-	455 / 1	-	455 / 1	650 / 1	649 / 1
	7:30 - 10:30	-	455 / 1	-	-	650 / 1	650 / 1
	16:00 - 20:00	-	-	-	-	-	-
	21:00 - 24:00	-	-	-	-	-	-

2.5. PRELIMINARY ANALYSES OF DATA

In order to provide better insight into the quality and characteristics of airborne imagery, a preliminary analysis is done on each of the data collections at hand. The mean contrast of the mine targets and the standard deviation of the images with mines are important statistical parameters that can provide a better picture of the quality of images and mine signatures and the kind of performance that can be expected for mine and minefield detection. The mean contrast of each mine type is a measure of the relative intensity of the mine in comparison with the background. The gray value contrast is calculated by taking the mean of a *1-pixel* radius around the mine target and subtracting the estimated gray value of the whole image.

If g_M is the mean of the *1-pixel* neighborhood, g_I is the mean of the image, then the gray value contrast $\overline{\mu}_M$ is given as

$$\overline{\mu}_M = g_M - g_I \tag{2.1}$$

The mean value for the mine target (g_M) is obtained as the maximum local value in the neighborhood of the specified ground truth for the mine. The mean value for the image (g_I) is obtained as the mean value of middle 50 percentile values of the image. The expression in equation 2.1 is valid as long as all the imagery taken into consideration for calculating the mean contrast for the mine target is imaged under the same level of illumination. But in reality, the runs under each band and in the same time-period range can be collected during different days of the week. The illumination during different days may be different due to various factors. Thus, while calculating the mean contrast for each mine type over different runs, the potential change in illumination should be accounted for. To do this, the expression in equation 2.1 is normalized with respect to the mean of the image g_I to obtain relative contrast. Thus, the normalized mean contrast is defined as:

$$\mu_M = \frac{g_M - g_I}{g_I} = \frac{g_M}{g_I} - 1 \tag{2.2}$$

The standard deviation of the mine signature ($\overline{\sigma}_M$) is calculated over the same neighborhood as the mean target value μ_M. A similar normalization as in the case of target contrast in performed. This gives a measure of the variation of intensity in and around the mine signature as:

$$\sigma_M = \frac{\overline{\sigma}_M}{g_I} \tag{2.3}$$

The standard deviation of the image frame ($\overline{\sigma}_I$) is an indicator of the amount of variation in the intensity of the background. The standard deviation for the image is also calculated for the middle 50 percentile values of the image frame. This can be a factor of the illumination and thus a similar normalization as discussed in equation 2.2 is done.

If $\overline{\sigma}_I$ is the standard deviation of the image, then defining a normalized standard deviation as

$$\sigma_I = \frac{\overline{\sigma}_I}{g_I} \tag{2.4}$$

In this manner, the mean contrast for each target and the normalized standard deviation for each image are calculated for different combinations of data collection, filter band and time of day. The main distinction that has to be made here is between daytime and nighttime images. Daytime images generally have bright mine signature and nighttime images have dark mine signature. This can be viewed as positive and negative contrast, respectively in relation to the background.

In order to calculate the mean contrast and standard deviation, the ground truth for each image frame is considered for the coordinates of each mine. But, in reality, there are numerous instances where the ground truth points to pixels in the surrounds of the mine target and not the actual center of the mine. This aberration can be attributed to human error, mine shadow during daytime and other visual artifacts. Thus, the correct location of the mine signature needs to be determined before computing the mean

contrast. The *1-pixel* neighborhood is chosen depending on the time of day. For example, mine signatures for daytime and nighttime are given as in Figure 2.1. During daytime, a mine signature looks like the image shown in Figure 2.1 (a). In this image, as it can be seen, the mine target is bright and the surroundings are relatively dark. This gives rise to positive contrast. Note that there is a significant shadow feature near the mine signature. However, the shadow feature is not representative of the target signature in general and has been neglected. Figure 2.1 (b) shows a typical signature of a mine at nighttime. Clearly the contrast in this case is negative.

In order to determine the correct neighborhood, the 1-pixel radius around the brightest pixel is considered for the daytime mine signature (Figure 2.1(a)) and the 1-pixel radius around the darkest pixel is considered for the nighttime mine signature (Figure 2.1(b)). The statistics for false alarms are also calculated. These false alarms are basically the ones generated by the anomaly detector algorithm but does not include the marked fiducials. The false alarms evaluted here are those primarily due to naturally occurring clutter. The number of false alarms (target locations) that are detected by the anomaly detector is generally very high compared to the number of mines. It would not be computationally efficient or logically necessary to calculate the statistics of all the false alarms that are detected. Therefore, a threshold is fixed on the number of false alarms for which the statistics should be calculated. In order to do this, a false alarm rate (3×10^{-2}) has been selected in the following evaluation.

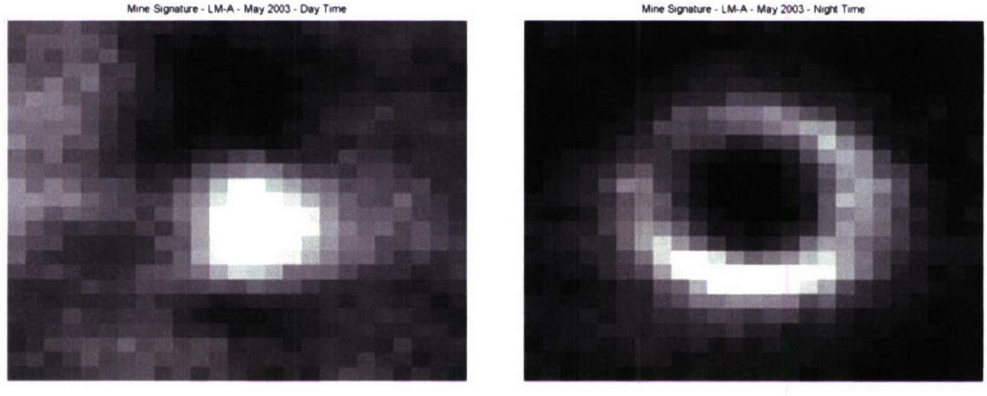

(a) Daytime (b) Nighttime

Figure 2.1. Mine Signature (LM_A) at Different Times of the Day - May 2003.

The number of false alarms to be allowed per image is calculated according to this rate, by multiplying the FAR with a fixed factor of the resolution of the image. This false alarm rate corresponds to approximately 7.5 false alarms per frame. The statistics for a selected number of false alarms per image alone are calculated. The mean contrast and standard deviation for the false alarm is calculated in a similar manner to the mines using 1-pixel neighborhood around the detected false alarm location. The mean contrast of the mines (along with false alarms) is tabulated. In addition to the mean contrast, the standard deviation of the mines and the standard deviation of the images with those mines are presented in the form of tables for each data collection categorized by band and time of day. The statistics across all the tables have been scaled by a constant factor of 10^4 for better readability. Since the false alarms can have both positive as well as negative contrast, the mean contrast value of the false alarms is calculated as the mean of the absolute value for all the selected false alarms.

In addition to presenting the mean contrast and the image standard deviation in the form of tables, box plots are drawn to show the variation of these statistics for each mine type. Box plots presented in Figures 2.2 – 2.16 display the lower and upper quartile of the parameters along with the median. In the box plots, the upper and lower edges of the boxes represent the upper and lower quartile of each mine's mean contrast and the red line inside the boxes represents the respective median values. The upper and lower whiskers (small horizontal lines) show the extent to which the values in the respective vectors extend. The occasional red '+' signs represent values that are outliers to the range of values taken for calculation. Box plots presented in such a fashion present a unique way of displaying a lot of information about the distribution of the data in a concise manner. The numbers next to each mine type in the x-axis, represent the number of each mine signatures available for computation. One more point to note is that, the mean contrast values are normalized as per the median of the image standard deviation in order to provide a common basis for comparison of data across different backgrounds, filter bands and time of day. The resulting number in the figure shows the expected signal to clutter ratio for each mine type and typical false alarms.

2.5.1. May 2002 Data. Table 2.10 shows the mine statistics for the May 2002 data. From these results, it can be seen that during daytime in the case of large surface

mines (LP_B and LM_A), the metallic mines show more contrast than the plastic or non-metallic mines, especially in Band 2 which is the solar band. The small mine SM_A has a very weak signature and consequently always has the lowest mean contrast amongst all the mines. The false alarms (denoted by FA) have values that can vary over a wide range and thus the mean contrast is not consistent. For the May 2002 data, it is seen that mines LM_A and LP_B (the large mines), have higher contrast than all the other mines, the metallic LM_A is stronger than the plastic LP_B during daytime showing that reflection plays a bigger role during daytime. However for nighttime (data available only for Band 1), LP_B (large plastic mine) shows higher contrast as compared to LM_A (large metal mine). The medium mine MP_A has relatively weaker contrast. The smaller mine SM_A has the lowest mean contrast.

Table 2.10. Mine Statistics for May 2002 Data (x 10^{-4}).

			LP_B	LM_A	MP_A	SM_A	FA
Band-1 (full)	03:00 - 04:30	μ_M	-224	-87	-47	-	57
		σ_M	11	11	16	-	11
		σ_I	70	32	70	-	64
	09:00 - 11:00	μ_M	355	471	322	19	358
		σ_M	29	37	33	15	29
		σ_I	45	43	57	39	53
	18:00 - 19:00	μ_M	176	218	62	80	29
		σ_M	11	13	11	11	11
		σ_I	37	53	29	36	43
	22:00 - 23:00	μ_M	-168	-68	-16	-78	66
		σ_M	10	9	9	7	10
		σ_I	39	35	39	38	40
Band-2 (solar)	09:00 - 11:00	μ_M	-	523	283	-	477
		σ_M	-	55	57	-	51
		σ_I	-	82	53	-	71
	18:00 - 19:00	μ_M	123	287	-	33	63
		σ_M	11	13	-	11	10
		σ_I	27	18	-	21	20
Band-3 (thermal 1)	09:00 - 11:00	μ_M	500	617	411	156	451
		σ_M	43	37	68	38	36
		σ_I	36	45	35	35	42
	18:00 - 19:00	μ_M	114	127	50	27	27
		σ_M	10	13	8	9	10
		σ_I	30	30	16	35	31
Band-4 (thermal 2)	09:00 - 11:00	μ_M	382	148	73	127	195
		σ_M	40	15	9	23	26
		σ_I	37	39	45	38	39
	18:00 - 19:00	μ_M	-	106	38	62	36
		σ_M	-	9	9	10	9
		σ_I	-	33	15	17	29

Figures 2.2 – 2.5 show the box plots for the May 2002 data collection arranged according to band and times of the day. Two times of the day 0900 – 1100 and 1800 – 1930 are shown side by side. Band 1 has got nighttime data also. Therefore, Figure 2.2 has four subplots each showing one time period for Band 1. The changes in the mean contrast variation can be easily observed across the plots signifying different times of the day. Contrast during daytime shows wider variation (as seen from the longer boxes in subplots (b) and (d) as compared to the nighttime data seen in subplots (a) and (c)) in Figure 2.2.

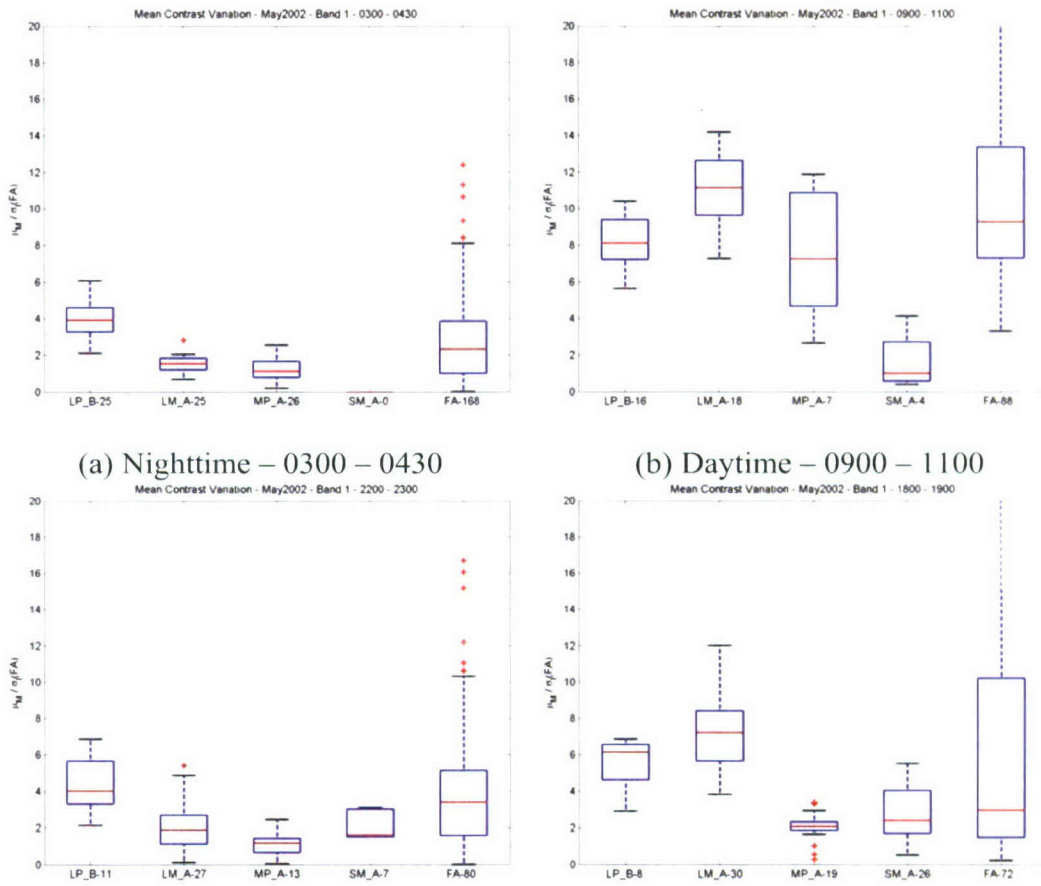

(a) Nighttime – 0300 – 0430 (b) Daytime – 0900 – 1100

(c) Nighttime 2200 – 2300 (d) Daytime – 1800 – 1900

Figure 2.2. Mean Contrast - May 2002 – Band 1.

As noted earlier from the table, during nighttime LP_B shows the best contrast while LM_A shows best contrast during daytime. Except for a few exceptions (like in Band 4), SM_A mine shows the lowest contrast.

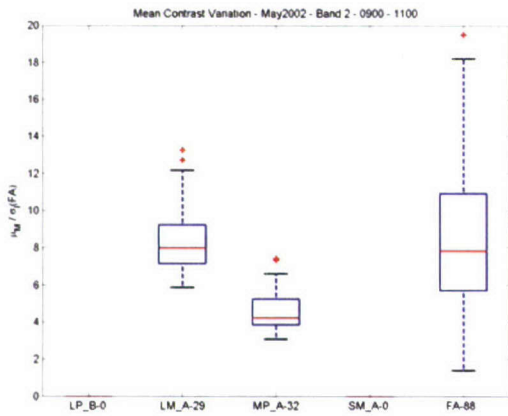

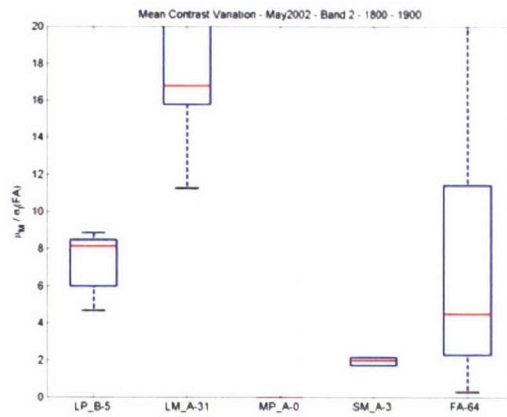

(a) Daytime – 0900 – 1100 (b) Daytime – 1800 – 1900

Figure 2.3. Mean Contrast – May 2002 – Band 2.

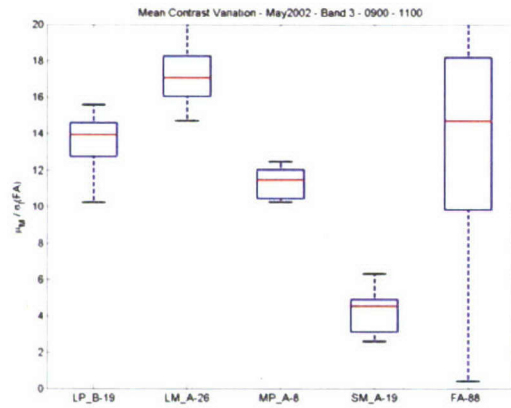

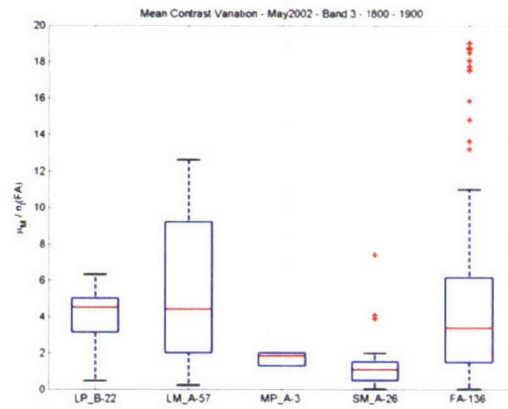

(a) Daytime – 0900 – 1100 (b) Daytime – 1800 – 1900

Figure 2.4. Mean Contrast – May 2002 – Band 3.

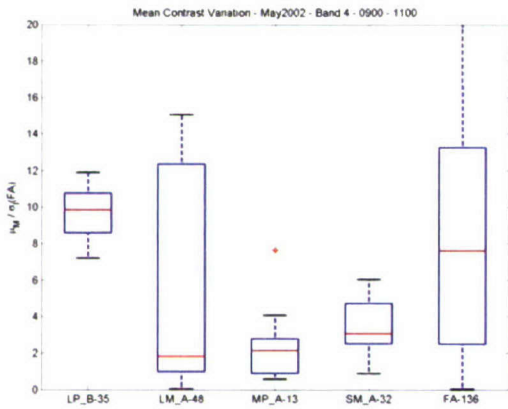

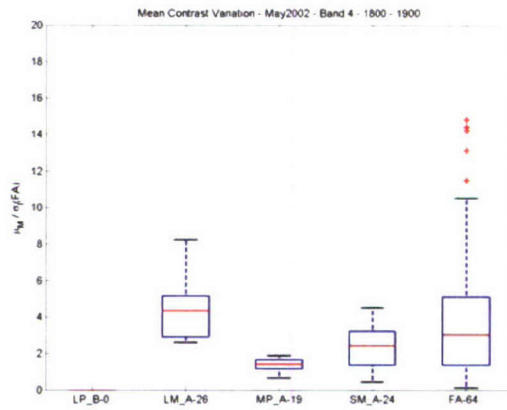

(a) Daytime – 0900 – 1100 (b) Daytime – 1800 – 1900

Figure 2.5. Mean Contrast – May 2002 – Band 4.

2.5.2. August 2002 Data. Table 2.11 shows the mine statistics for the August 2002 data. The August 2002 data has got an even distribution of data in both day and nighttime conditions. Again during daytime, the large metallic mine (LM_A) has got better contrast as compared to the plastic mine (LP_B). The smallest mine (SM_A) provides better contrast during daytime in Band 0 than any other time or band. In terms of signal to contrast, nighttime performance is lower than daytime as contrast during nighttime is primarily due to the thermal contrast of the mines. However, the contrast for the false alarms is lower as well and hence the relative performance during daytime and nighttime may be comparable. In the case of nighttime data, the plastic mines respond better than the metallic mines and thus the large mine (LP_B) has better contrast during nighttime than the large metallic mine (LM_A). Similarly, the medium plastic mine MP_A also has good contrast compared to the metallic mines.

Table 2.11. Mine Statistics for August 2002 Data (x 10^{-4}).

			LP_B	LM_A	MP_A	SM_A	FA
Band - 0 (full)	00:00 - 01:30	μ_M	-149	-119	-191	-17	30
		σ_M	11	10	22	13	17
		σ_I	60	76	114	88	87
	18:00 - 19:30	μ_M	524	1452	458	583	504
		σ_M	54	113	77	75	57
		σ_I	70	72	112	70	88
Band - 1 (full)	03:00 - 04:30	μ_M	-99	-90	-97	-26	48
		σ_M	6	5	8	6	7
		σ_I	11	20	18	13	22
	08:00 - 09:30	μ_M	409	580	336	217	471
		σ_M	37	29	68	46	45
		σ_I	70	72	79	82	69

Figures 2.6 – 2.7 show the box plots for the August 2002 data collection arranged according to band and times of the day. Two times of the day 0000 – 0130 (nighttime) and 1800 – 1930 (daytime) for Band 0 and 0300 – 0430 (nighttime) and 0800 and 0930 (daytime) for Band 1 are shown side by side in Figures 2.6 and 2.7, respectively. Same kind of trend as earlier can be noticed here as well. Daytime contrast shows wider variations as compared to nighttime signature. LM_A mines show significantly better contrast during daytime as compared to other mines.

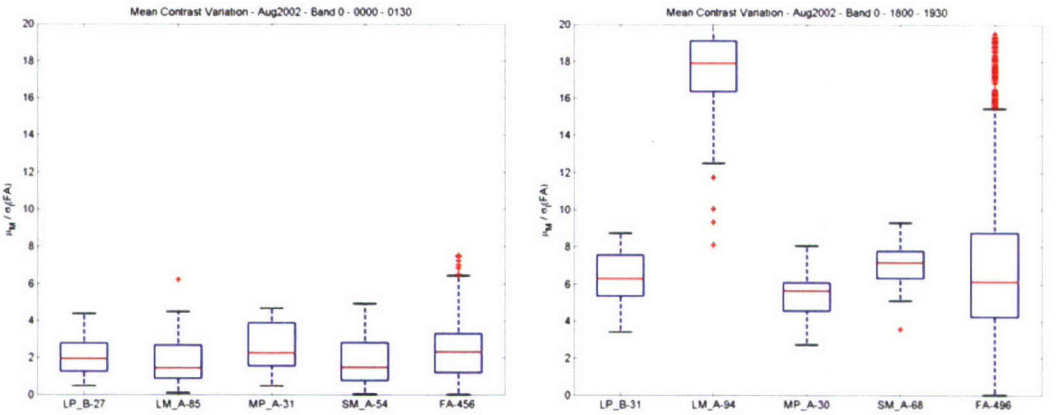

(a) Nighttime 0000 – 0130 (b) Daytime – 1800 – 1930

Figure 2.6. Mean Contrast – August 2002 – Band 0.

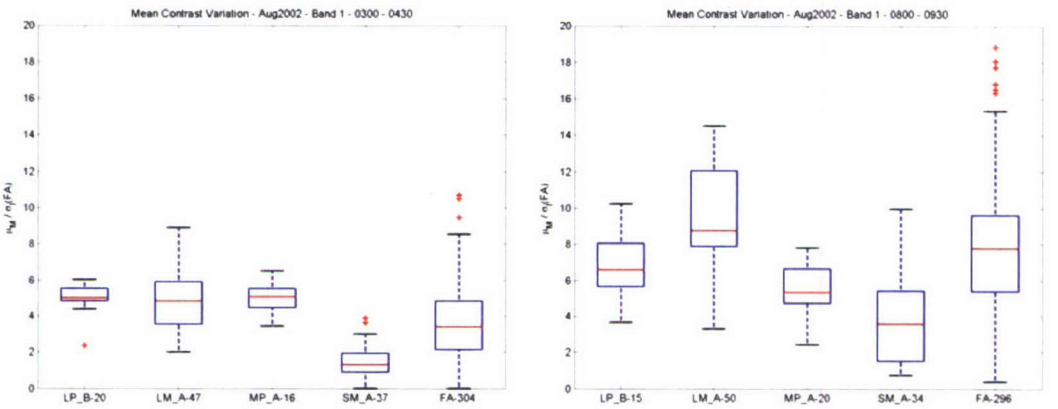

(a) Nighttime 0300 – 0430 (b) Daytime – 0800 – 0930

Figure 2.7. Mean Contrast – August 2002 – Band 1

2.5.3. October 2002 Data. Table 2.12 presents the statistics for the October 2002 data collection. A similar trend for the contrast is found here. But the signatures found in this collection seem to be much better in contrast than the data collections discussed previously. One reason for this higher contrast is the difference in the background found in this data collection to the backgrounds found in the earlier collections. At the same time, the contrast for the false alarms is also appreciably higher. This collection of data does not have nighttime data and thus there are no time zones for nighttime indicated. Since the data collected is daytime data, the metallic mines offer much higher contrast than the plastic mines as expected.

Figures 2.8 – 2.11 show the box plots for the October 2002 data collection arranged according to band and times of the day. Two times of the day 1000 – 1200 and

1500 – 1700 for Bands 1, 2 and 3 are shown side by side. For Band 4, 1000 – 1200 alone is available and so it is shown in a separate figure. One observation that can be made is that the distribution of the mean contrast values of the mines is quite similar between the two time periods under consideration. This can be attributed to the fact that the contrast due to reflection is the only factor taken into consideration since both the time periods are in broad daylight. Because of this, the contrast offered by the metallic mines is prominent for most bands and time periods.

Table 2.12. Mine Statistics for October 2002 Data (x 10^{-4}).

			LP_B	LM_A	MP_A	SM_A	FA
Band-1 (full)	10:00 - 12:00	μ_M	1298	1744	989	642	912
		σ_M	73	71	73	69	72
		σ_I	123	134	124	134	122
	15:00 - 17:00	μ_M	770	1006	526	478	418
		σ_M	60	65	76	50	40
		σ_I	116	116	122	116	115
Band-2 (solar)	10:00 - 12:00	μ_M	782	702	564	434	480
		σ_M	73	43	51	39	40
		σ_I	150	137	121	137	129
	15:00 - 17:00	μ_M	320	643	254	327	298
		σ_M	23	52	28	26	26
		σ_I	43	43	42	43	46
Band-3 (thermal 1)	10:00 - 12:00	μ_M	771	1034	521	376	657
		σ_M	45	47	44	53	51
		σ_I	83	87	96	87	86
	15:00 - 17:00	μ_M	505	643	249	346	467
		σ_M	23	42	33	32	32
		σ_I	58	56	51	56	55
Band-4 (thermal 2)	10:00 - 12:00	μ_M	427	677	409	207	502
		σ_M	32	31	25	28	35
		σ_I	62	65	63	65	56

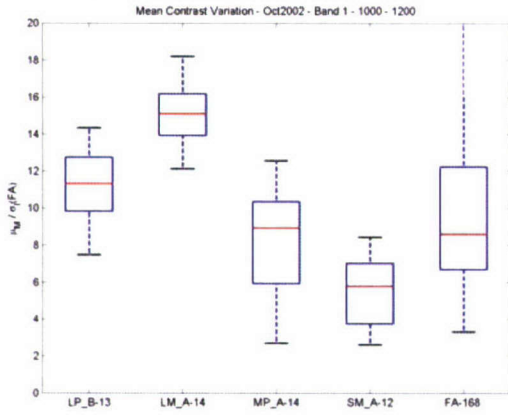

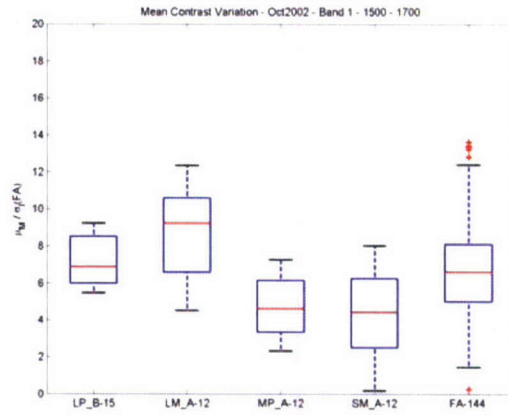

(a) Daytime – 1000 – 1200 (b) Daytime – 1500 – 1700

Figure 2.8. Mean Contrast – October 2002 – Band 1.

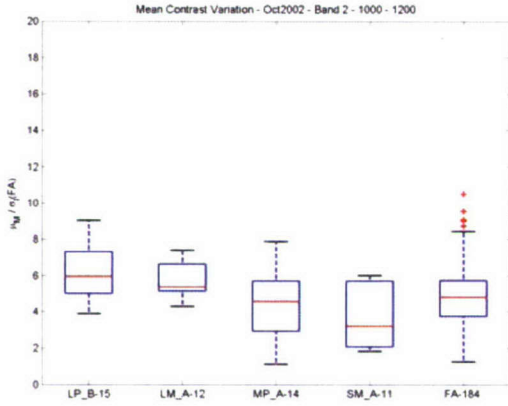

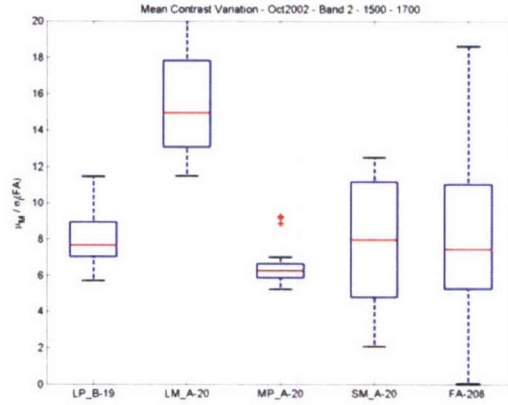

(a) Daytime – 1000 – 1200 (b) Daytime – 1500 – 1700

Figure 2.9. Mean Contrast – October 2002 – Band 2.

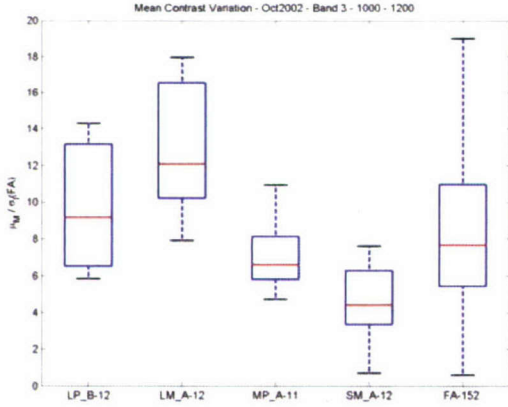

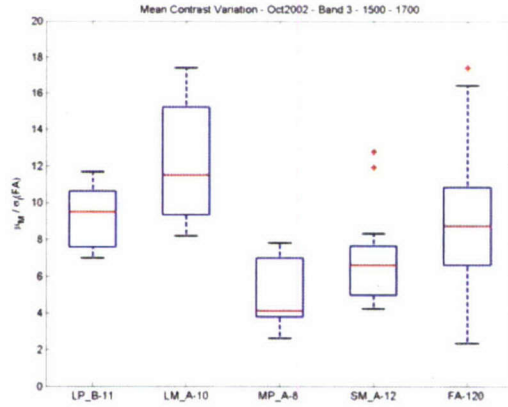

(a) Daytime – 1000 – 1200 (b) Daytime – 1500 – 1700

Figure 2.10. Mean Contrast – October 2002 – Band 3.

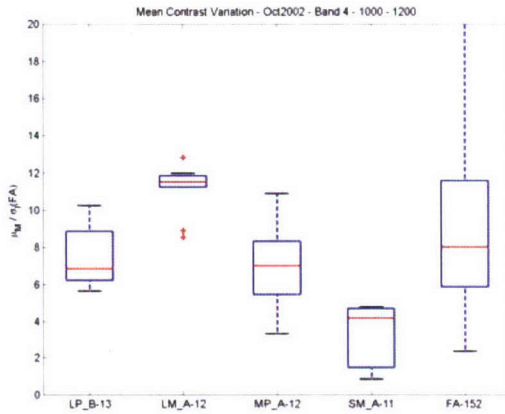

Daytime 1000 – 1200
Figure 2.11. Mean Contrast – October 2002 – Band 4.

2.5.4. May 2003 Data. Table 2.13 gives the mine statistics for the May 2003 data collection. Keeping with the trend noticed till now, the large metallic mine (LM_A) is one of the strongest in contrast during daytime, closely followed by the other large mine (LP_B) and the medium mine (MP_A). Noticeably, this data collection has no runs present for Band 2 nighttime. Only two time periods have been considered for display in this work due to the abundance of data found in these time periods and also for sake of brevity. They are 2:30 – 5:30 and 7:30 – 10:30. Band 0 in this data collection has fewer runs in the time periods chosen and so the statistics for Band 0 are omitted from the tabulation.

Figures 2.12 – 2.15 show the box plots for the May 2003 data collection arranged according to band and times of the day. Two times of the day 0230 – 0530 (nighttime) and 0730 – 1030 (daytime) for Bands 1, 3 and 4 are shown side by side. For Band 2, 0730 – 1030 alone is available and so it is shown in a separate figure. In this data collection it can be observed that the contrast variation is very consistent across the different bands and the different times of the day. Wider variation in the range of values for each mine type is observed during daytime statistics than nighttime. The small metal mine SM_A is the mine with the weakest contrast in all the cases.

Table 2.13. Mine Statistics for May 2003 Data (x 10^{-4}).

			LP_B	LM_A	MP_A	SM_A	FA
Band-1 (full)	02:30 - 05:30	μ_M	-183	-99	-140	-33	87
		σ_M	7	9	19	7	10
		σ_I	18	19	18	19	24
	07:30 - 10:30	μ_M	397	470	270	59	284
		σ_M	43	58	38	15	36
		σ_I	45	45	39	46	48
Band-2 (solar)	02:30 - 05:30	μ_M	-	-	-	-	-
		σ_M	-	-	-	-	-
		σ_I	-	-	-	-	-
	07:30 - 10:30	μ_M	268	259	133	45	221
		σ_M	30	38	24	14	37
		σ_I	26	26	25	26	31
Band-3 (thermal 1)	02:30 - 05:30	μ_M	-176	-113	-147	-21	84
		σ_M	7	10	17	7	9
		σ_I	14	17	16	17	19
	07:30 - 10:30	μ_M	300	405	220	43	303
		σ_M	32	40	32	13	31
		σ_I	43	43	40	43	46
Band-4 (thermal 2)	02:30 - 05:30	μ_M	-136	-82	-99	-29	66
		σ_M	7	8	13	7	8
		σ_I	13	13	13	13	15
	07:30 - 10:30	μ_M	213	307	154	43	242
		σ_M	24	28	24	11	25
		σ_I	39	37	32	37	38

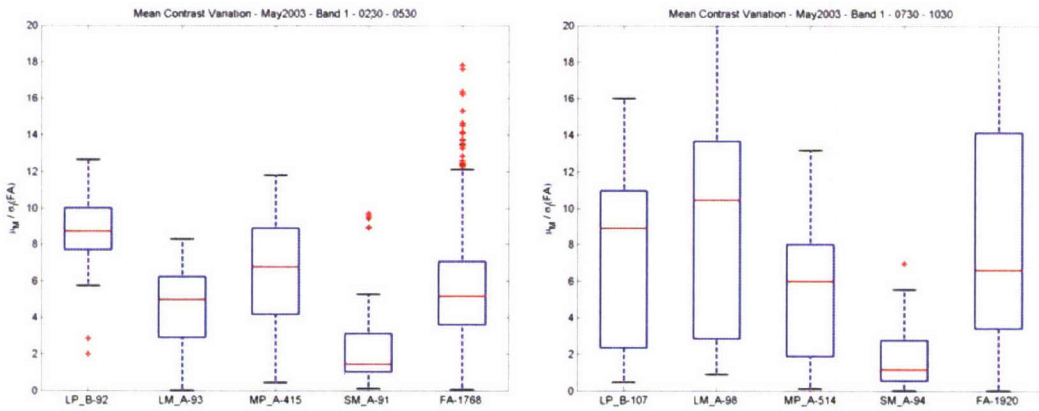

(a) Nighttime 0230 – 0530 (b) Daytime – 0730 – 1030

Figure 2.12. Mean Contrast – May 2003 – Band 1.

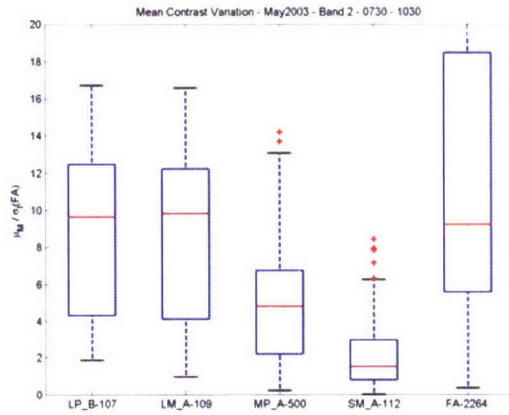

Daytime – 0730 – 1030

Figure 2.13. Mean Contrast – May 2003 – Band 2.

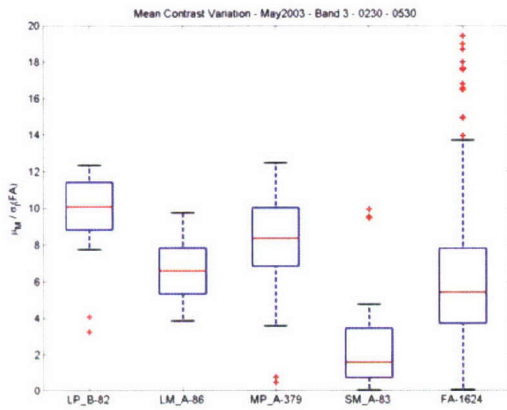

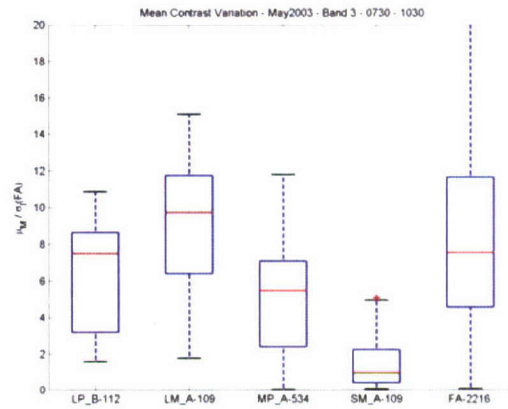

(a) Nighttime 0230 – 0530 (b) Daytime – 0730 – 1030

Figure 2.14. Mean Contrast – May 2003 – Band 3.

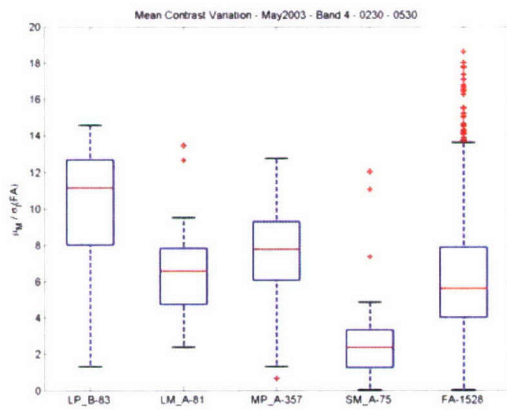

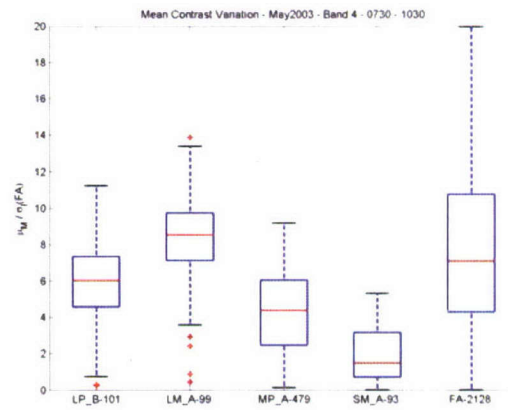

(a) Nighttime 0230 – 0530 (b) Daytime – 0730 – 1030

Figure 2.15. Mean Contrast – May 2003 – Band 4.

3. ANOMALY DETECTOR AND DETECTION ARCHITECTURE

The primary aim of this section is to explain in detail the anomaly detector that is integral to the work presented in this thesis. A basic assumption that is made here is that the target signatures (mines) are statistically different from the local background. This assumption translates to the idea that such targets can be identified as local anomalies in the image. A test statistic that is designed to detect such anomalies is called an anomaly detector. The anomaly detector under consideration for this work is the RX algorithm that was proposed by Reed and Yu [22]. In particular, the motivation here is the RX implementation as proposed by Holmes [21] et al. The rest of the chapter contains the introduction to the detection architecture used, a brief survey of the anomaly detectors, a detailed theoretical look at the RX algorithm and the theory behind non-max suppression. This is followed by a simulation example of the detection architecture and the basic idea leading to the work done in the next chapter.

3.1. DETECTION ARCHITECTURE

The block diagram in Figure 3.1 shows the overall detection architecture implemented here. The detection architecture and its functional blocks are discussed briefly in this section. A more detailed explanation of some of the important blocks is presented in the later sections.

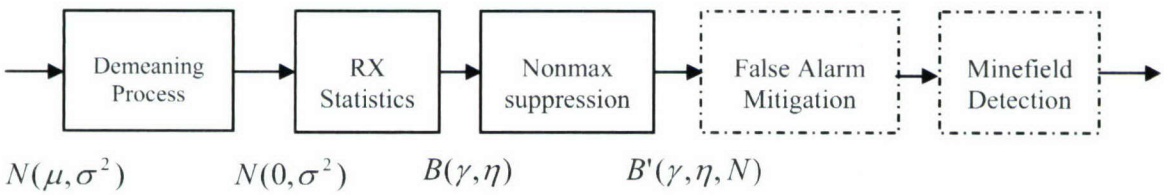

Figure 3.1. Detection Architecture for Airborne Mine and Minefield Detection.

The RX algorithm makes an assumption that the images that are available to it are zero mean, uncorrelated and Gaussian distributed. The Gaussian distribution of the gray values is a fair assumption for most electro-optical sensors (although a lot of images are not truly Gaussian distributed). Images by definition are not zero mean; however, the

imagery data can often be assumed to have a slowly varying mean value. A locally zero mean image, can be obtained by subtracting a non-stationary local mean from the image. In order to achieve this, a properly sized averaging mask is convolved with the original image and then the convolution sum is subtracted from the original image. If W_R is the averaging mask (of size approximately equal to the background mask of RX as proposed by Holmes [21] et al.) and $I_{M,N}$ is the original image data which is locally Gaussian distributed with quasi-stationary mean value ($I_{M,N} \in N(\overline{\mu}, \sigma^2)$), then the zero mean input image for RX, $I^*_{M,N}$, is obtained as

$$I^*_{M,N} = I_{M,N} - I_{M,N} * W_R \tag{3.1}$$

Here, the image is of dimensions M x N and W_R is the averaging mask of radius R. After the demeaning process, the resulting image $I^*_{M,N}$ is zero mean Gaussian distributed ($N(0, \sigma^2)$). This zero mean image is passed through the RX anomaly detector. A detailed explanation of the RX anomaly detector is presented in Section 3.3. The RX detector image provides a statistical measure for the presence of an anomaly at each pixel location. Local maximum in a given neighborhood on the RX statistic image can be considered as viable anomalies. Non-max suppression can be viewed as a thresholding process that lets only the maximum valued target survive in a local neighborhood of certain size. A detailed explanation of the working of non max suppression is presented in Section 3.4.

A false alarm is an object in the background of the image that is detected by the anomaly detector but is not a mine target. The anomaly detector detects these objects because of the high statistical contrast from the background. In most cases, the shape and other attributes of false alarms may not be similar to the mine targets. A false alarm mitigation scheme is designed to discriminate between various mine shapes and reject such unwanted false alarms. The details of this scheme are out of the scope of this thesis. Some results for false alarm mitigation for May 2002 data can be found in [23].

The final block in the airborne minefield detection architecture is minefield detection. As the name signifies, minefield detection involves the detection and

localization of minefields using the mine target information obtained after false alarm mitigation. Minefields can be classified as patterned, scattered and nuisance minefields. The discussion of minefield detection algorithms is again not within the limits of this thesis. More information on minefield detection can be found in [24] and [25].

3.2. SURVEY ON ANOMALY DETECTION

The purpose of this section is to present a brief survey of the anomaly detectors that have been implemented and are being researched in the industry and academics. As far as mine detection is concerned, the RX anomaly detector [22] is probably the most popular algorithm, a sort of benchmark for other anomaly detectors. A modification [21] of the same has been implemented by Holmes et al. for the COBRA [16] program. Gauss Markov Random Fields (GMRF) based anomaly detector has been explored for hyperspectral imagery by Moura et al. [15]. The primary advantage of the GMRF anomaly detector over other Maximum Likelihood (ML) detectors is that it is computationally less expensive. The primary reason is that the computationally costly inversion of the covariance matrix that is done for multiple band images (like hyperspectral images) is avoided by the GMRF detector. Other anomaly detector is, the Estimator – Correlator (EC) detector based on a matched filter approach being explored by Baertlain et al. [26]. This anomaly detector makes use of a matched filter based on a Weiner filter implementation, to detect the specified spatial signature in the presence of correlated noise. An anomaly detector based on the wavelet transform was proposed by Reed et al. [27]. This algorithm is used for multi-spectral object detection. The second moment of the wavelet transform is computed in order to develop a suitable test function for the generalized likelihood ratio test (GLRT) using which the detection statistic is computed.

Anomaly detection can be performed with the help of stochastic mixture modeling. Stochastic mixture modeling assumes a mixing of more than one probability density function, for example, Gaussian mixtures with different moments. Stein [28] makes use of a stochastic compositional model (SCM) for the modeling and subsequent detection for hyperspectral imagery. SCM models each input vector of multivariate data as a linear combination of normally distributed random variables. Mixing parameters and

shape parameter of the components of the model are estimated with the help of the Expectation – Maximization technique and consequently a log likelihood ratio is formed for the model and anomaly detection done.

An anomaly detector of particular interest is an anomaly detector based on the segmentation of the background clutter. Fosgate et al. [29] talk about a multiscale segmentation approach to classify the clutter, especially grass and forest in order to improve the automatic target recognition performance of SAR (Synthetic Aperture Radar) imagery. Much similar to the background analysis presented in this thesis, the characteristic statistical differences between different background terrains is used as a function of the scale. Models for each background are developed and these are used to accomplish pixel classification and segmentation. Based on this particular classification, the usual likelihood ratio tests are developed and anomaly detection performed.

Stochastic Expectation Maximization (SEM) is a similar approach to SCM explained above. Beaven, Stein and Hoff [30] use SEM to estimate the parameters of a Gaussian mixture models and then compare this model with a linear mixture model for hyperspectral data and thereby perform anomaly detection for both types of mixture models in a similar fashion to the SCM approach [28]. SEM is similar to expectation maximization but for the stochastic element, which improves the convergence properties of the algorithm.

3.3. THE RX ANOMALY DETECTOR

The RX algorithm as implemented by Holmes et al. [21] uses a set of three masks, viz., the target mask, the blanking mask and the demeaning mask. Figure 3.2 shows the geometry of the three masks used in the current computation. The target mask governed by the target radius, defines the shape of the target, which is assumed to be circular in this case. The background mask governed by the demeaning radius, defines the background area that is used to estimate of the local mean and is used for the demeaning of the raw image. The background statistics are computed over the annular region between the background radius and the blanking radius. The blanking radius is used to reject any pixels in the neighborhood of the potential target (at the center) from the calculation of the background statistics. The target and the background masks are disjoint and give out

fair estimates of the target statistics and the background statistics, respectively. The RX algorithm accepts the raw image as input and calculates the convolution of the image with the set of masks mentioned. The current implementation of the RX algorithm is computed in the frequency domain, thus making use of the fast Fourier transform (FFT) for computational efficiency. RX algorithm for a scalar valued image data effectively results in the computation of signal to clutter ratio over the image. The RX response provides an image equal in size to the original image which has values of the signal to clutter at each pixel location.

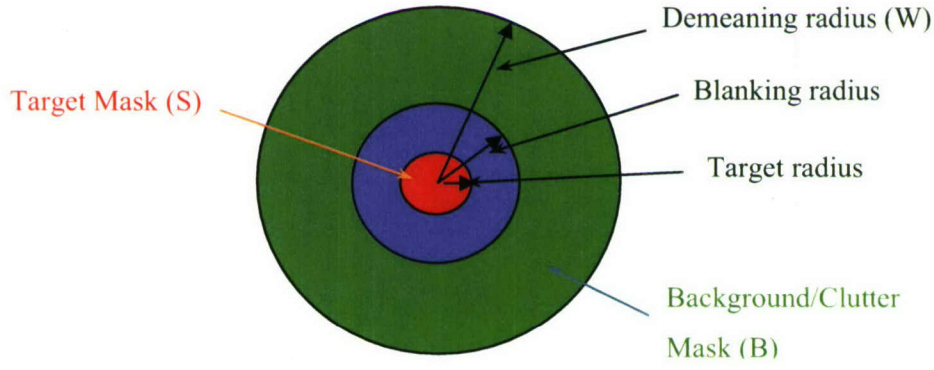

Figure 3.2. Geometric Representation of the Three Masks Used for RX Anomaly Detection.

The RX algorithm as suggested by Reed and Yu [22] is generally applicable for multi-band images with zero mean, uncorrelated Gaussian background. For an image $I(i,j) = I_l$, the RX statistics $r_X(i,j)$ for a J band image is given by:

$$r_X(i,j) = N_T\left(\mu_S^T M^{-1} \mu_S\right) \tag{3.2}$$

where M is the locally estimated covariance matrix of dimension J x J given by

$$M = \frac{1}{N_C} \sum_{l \in W_C} I_l^T I_l ,$$

μ_S is the mean target signature given by

$$\mu_S = \frac{1}{N_T} \sum_{l \in W_T} I_l$$

where . N_C and N_T are the number of clutter and target pixels used in estimating M and μ_S, respectively.

The present usage of the RX algorithm is only for single band data and therefore, $J = 1$. The RX statistic in this case is given as

$$r_X = N_T \left(\frac{\left(\frac{1}{N_T} \sum_{j \in W_T} I_j \right)^2}{\frac{1}{N_C} \sum_{i \in W_C} I_i^2} \right) \tag{3.3}$$

The primary assumption made by Reed and Yu in [22] is that the background is zero-mean uncorrelated Gaussian. Under this assumption, the probability density functions obtained by Reed and Yu [22] for the RX statistic for background and the target are given by,

$$f(x \mid H_0) = \frac{\Gamma\left(\frac{N}{2}\right)}{\Gamma\left(\frac{N-J}{2}\right)\Gamma\left(\frac{J}{2}\right)} (1-x)^{\left(\frac{N-J}{2}\right)} x^{\left(\frac{J-2}{2}\right)}, \tag{3.4}$$

for $0 < x < 1$

$$f(x \mid H_1) = \frac{\Gamma\left(\frac{N}{2}\right)}{\Gamma\left(\frac{N-J}{2}\right)\Gamma\left(\frac{J}{2}\right)} . (1-x)^{\left(\frac{N-J-2}{2}\right)} x^{\left(\frac{J-2}{2}\right)} e^{(-a/2)} \cdot {}_1F_1\left(\frac{N}{2}; \frac{J}{2}; \frac{ax}{2}\right) \tag{3.5}$$

for $0 < x < 1$

where $f(x \mid H_0)$ is the probability density function for x given that it is not a mine target and $f(x \mid H_1)$ is the probability density function given that the pixel location belongs to a mine.

In this system of equations, x is the transformed RX statistic (the so-called test function value), i.e. if r is the test statistic as obtained in equations 3.2 and 3.3, then

$$x = \frac{r}{r+1}, \qquad r \in [0,\infty), \qquad x \in [0,1] \tag{3.6}$$

N and J are parameters used to characterize the probability density which represents the number of samples and dimensions of the image, respectively. Also a is the generalized SNR given by,

$$a \approx \left(b^T M^{-1} b\right) \|W_T\|^2 \tag{3.7}$$

where b is the unknown signal intensity. In equation 3.5, ${}_1\mathrm{F}_1(a;b;z)$ is the confluent hypergeometric function [31]. From equation 3.4 it is seen that the probability density function for the RX statistic under null hypothesis is a beta density function, $B(\gamma,\eta)$ as

$$B(\gamma,\eta) = \frac{\Gamma(\gamma+\eta)}{\Gamma(\gamma)\Gamma(\eta)} x^{(\gamma-1)}(1-x)^{(\eta-1)}, \quad \gamma > 0,\ \eta > 0 \text{ and } 0 < x < 1 \tag{3.8}$$

where $\gamma = \frac{J}{2}$ *and* $\eta = \frac{N-J}{2}$

3.4. NON-MAX SUPPRESSION

The output of the RX algorithm can be called the "signal-to-clutter" image and it is of the same size as the original raw image. This image is subject to non-maximal suppression in order to get a list of targets that have been highlighted by the anomaly detector. This so called target-list consists of the coordinates of the potential targets along with the RX test statistic as per equation 3.3. Non-maximal suppression is a processing

algorithm that suppresses (makes zero) all the targets in a specific neighborhood (M-pixel radius) except the local maximum. The operation of non-maximal suppression can be explained in detail with the help of Figure 3.3. For each target at location *l(i,j)* (marked by 'X') consider a local neighborhood of radius M. The targets that are present inside this neighborhood alone are considered for non-maximal suppression. The central target at location *l* is set to zero if its RX statistic value is not the maximum in this neighborhood, else it is left as is. In this fashion, the M-pixel neighborhood is moved over the entire image and the local maxima selected. A list of these local maximum values along with the row and column information forms the targetlist for that particular image frame.

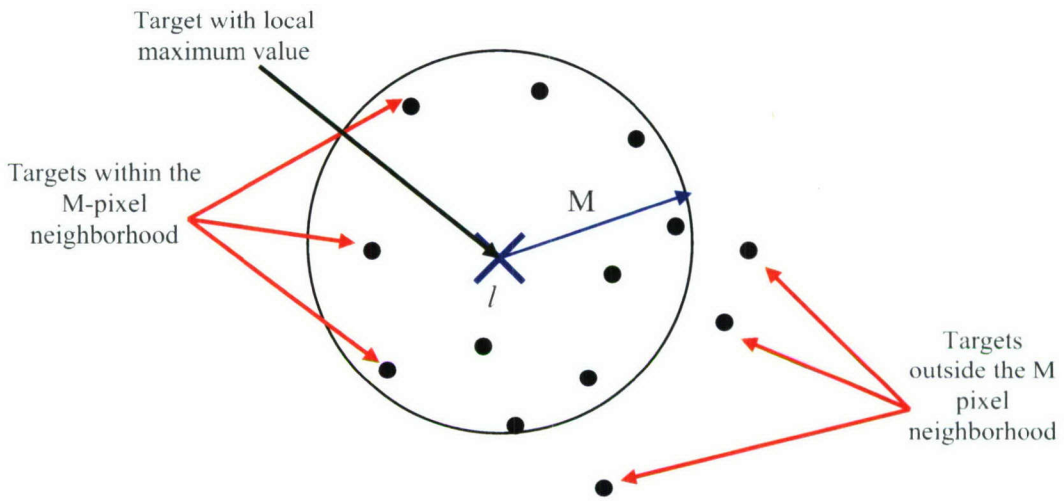

Figure 3.3. M-pixel Neighborhood Showing Potential Targets

As in the case of the RX statistics output, the probability density function for the distribution of RX statistics after non-max suppression under null and non-null hypothesis is of particular interest. The following mathematical derivation tries to estimate the probability density function for the RX statistics under null hypothesis after non-max suppression. Let $f(x|H_0)$ be the probability density function of the RX clutter statistic x. Let the function $g(l)$ represent the mapping function performed by the non-max operation and W_M be the M-pixel neighborhood.

Thus,

$$g(l) = \begin{cases} 1 & if \;\; x_l = X_l \equiv \text{local maximum in } \mathrm{W_M} \\ 0 & elsewhere \end{cases} \tag{3.9}$$

Let, $f(g(l)=1 \mid x)$ be the probability that the target at location l will take a value '1', given that its test statistic value is x. The probability density of the background statistics after non-max suppression is $f(x \mid g(l)=1, H_0)$.

Using Bayes' Rule,

$$f(x \mid g(l)=1, H_0) = \frac{f(x \mid H_0).f(g(l)=1 \mid x)}{f(g(l)=1)} \tag{3.10}$$

$$= \frac{f(x \mid H_0).f(g(l)=1 \mid x, H_0)}{\int_0^\infty f(x \mid H_0).f(g(l)=1 \mid x, H_0)dx} \tag{3.11}$$

The probability that any target value x survives also depends on the number of targets 'n_g' present in the neighborhood chosen for the non-max operation. The number of potential targets in a given neighborhood around a given target location, say n_g, is a random process that can be assumed to take on a Poisson distribution [32]. The density function obtained in equation 3.4 should account for this random number n_g and the non-max suppression process as discussed earlier. The Poisson probability density, is given in equation 3.12.

$$P(n_g) = \frac{e^{-\theta A}(\theta A)^{n_g}}{n_g!} \tag{3.12}$$

where A is the area of the neighborhood W_M and θ is the density of the potential targets. Now $f(g(l)=1 \mid \bar{x}, n_g = \bar{n})$ is the probability that the location l will take a value 1 given that its test statistic value is $\bar{x}$ and it has $\bar{n}$ potential targets in the local neighborhood of

W_M. This condition will occur only if every other target (at locations $m \in W_M$) in the neighborhood has a value less than the value present at location *l*, i.e. $\bar{x}$. This probability is given by:

$$f(x < \bar{x} \mid H_0) = \int_0^{\bar{x}} f(x \mid H_0)dx = F_{H_0}(\bar{x}) = CDF\ of\ x\ at\ \bar{x} \tag{3.13}$$

Thus, for $\bar{n}$ targets in the neighborhood $f(g(l) = 1 \mid \bar{x}, n_g = n_0)$ can be represented as,

$$f(g(l) = 1 \mid \bar{x}, n_g = \bar{n}) = \left(F(\bar{x})\right)^{\bar{n}}$$

The probability $f(g(l) = 1 \mid \bar{x})$ is given by:

$$f(g(l) = 1 \mid \bar{x}) = \sum_{\bar{n}=0}^{\infty} \left(F(\bar{x})\right)^{\bar{n}} P(\bar{n}) \tag{3.14}$$

$$= \sum_{\bar{n}=0}^{\infty} \left(F(\bar{x})\right)^{\bar{n}} \frac{e^{-\theta A}(\theta A)^{\bar{n}}}{\bar{n}!} \tag{3.15}$$

$$= \sum_{\bar{n}=0}^{\infty} \frac{(F(\bar{x})\theta A)^{\bar{n}} e^{-\theta A} . e^{-\theta A F(\bar{x})} . e^{+\theta A F(\bar{x})}}{\bar{n}!}$$

$$= \left[\sum_{\bar{n}=0}^{\infty} \frac{(F(\bar{x})\theta A)^{\bar{n}} . e^{-\theta A F(\bar{x})}}{\bar{n}!}\right] . e^{-\theta A(1 - F(\bar{x}))}$$

$$= e^{-\theta A(1-F(\bar{x}))} \tag{3.16}$$

The last step follows since,

$$\left[\sum_{\bar{n}=0}^{\infty} \frac{(F(\bar{x})\theta A)^{\bar{n}} . e^{-\theta A F(\bar{x})}}{\bar{n}!}\right] = 1$$

Thus,

$$f(g(l) = 1 \mid \bar{x}) = e^{-\theta A(1 - F(\bar{x}))} \tag{3.17}$$

Using equation 3.17 in 3.11, the probability density function used to model the background clutter statistics after non-max suppression is given by:

$$f(x \mid g(l)=1) = \frac{f(x \mid H_0).e^{-N(1-F(x))}}{\int_0^{\infty} f(x \mid H_0).e^{-N(1-F(\bar{x}))}dx} \tag{3.18}$$

where $f(x \mid H_0)$ is the probability due to RX statistics under null hypothesis and $N = \theta A$ is the expected number of independent targets present in the neighborhood W_M.

4. RX STATISTICS UNDER CORRELATED BACKGROUND

The airborne minefield detection system is expected to detect possible mines and minefields over various types of terrains, different soil conditions and at different times of the day. This raises the question as to what kind of detection performance can be achieved over different background (terrain) and whether the performance will be invariant to background characteristics. A basic knowledge of an anomaly detector [33] such as the RX algorithm should point to the fact that the performance over different types of background would differ as a factor of the spatial correlation and local inhomogeneities in the image. In order to quantify this performance, it becomes necessary to model the detection statistics of the anomaly detector into probabilistic models that gives more insight into the performance of the anomaly detector. In this section, the modeling of the background statistics alone is discussed for the case of uncorrelated background data.

4.1. A PROBABILISTIC MODEL FOR THE BACKGROUND STATISTICS

The particular variety of terrain found in the May 2003 data alone warrants the need for an in-depth study of the background and its effect on the anomaly detector performance. In order to better comprehend the effect of the background on detector performance, the values of the RX test statistics can be modeled using a parametric probabilistic model and the parameters of this model can be estimated from the available data. In the following, generalized 3-parameter beta density function [34] is considered to model RX statistics under null-hypothesis. The 3-parameter beta density is given by:

$$f_3(x|H_0) = \frac{\lambda^\gamma x^{\gamma-1}(1-x)^{\eta-1}}{B(\gamma,\eta)[1-(1-\lambda)x]^{\gamma+\eta}} \quad , \quad 0 \le x \le 1; \gamma, \eta, \lambda > 0 \tag{4.1}$$

The fundamental difference between the standard beta density function and the generalized 3-parameter beta distribution is the introduction of the third parameter λ. In statistical modeling, a very important property is the variety of shapes that a distribution can take. In general, a wider variety of shapes results in better modeling [34]. The

presence of λ in the 3-parameter beta distribution introduces more shapes that the function can take than the standard beta density. This is because the shape defining moments of a distribution, the mode, skew and kurtosis are dependent on λ as well as the other two parameters. The 3-parameter beta density function is defined for the test statistic x over the interval (0, 1). Some of the common shapes [35] for different parameter values that the 3 parameter beta distribution can take are shown in Figure 4.1. The parameters used are shown in the legend of Figure 4.1 are ordered as (γ, η ; λ).

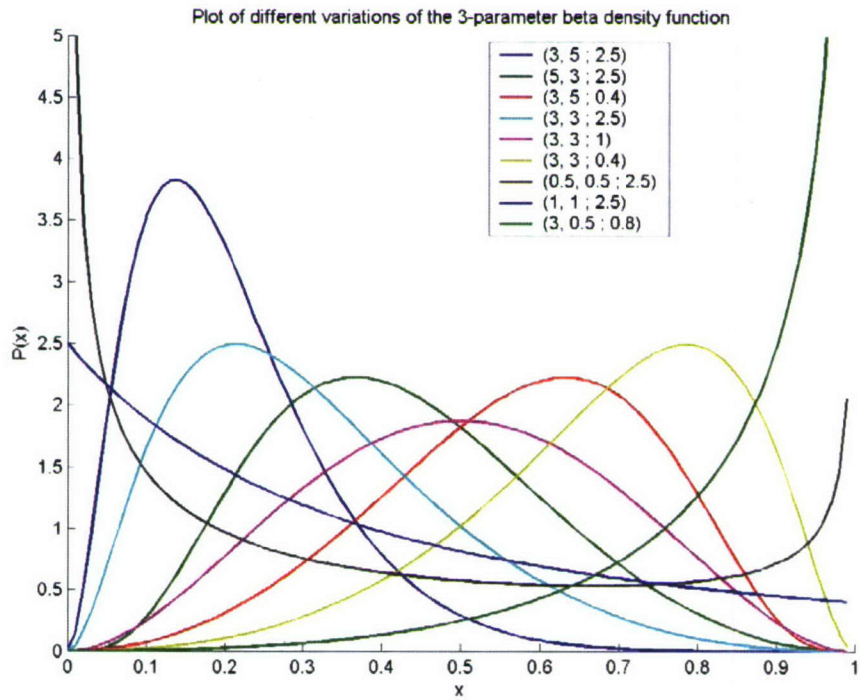

Figure 4.1. Various Forms of the 3-Parameter Beta Distribution.

In the following, it is assumed that the RX statistics for the background only images for different backgrounds follow a generalized beta density function as shown in equation 4.1. But, as per the theory derived in section 3.5 for background statistics after non-max suppression, a slight modification is introduced to equation 4.1, and the actual density function to be modeled is the expression in equation 4.2 given by:

$$f(x) = \frac{1}{\mathrm{K}} f_3(x) e^{-N(1-F_3(x))} \tag{4.2}$$

where $F_3(x)$ is the cumulative distribution function of $f_3(x)$, the 3-parameter beta distribution in equation 4.1 and $K = \int_0^1 f_3(x) e^{-N(1-F_3(x))} dx$. Note that the probability density function in equation 4.2 is defined for four parameters viz., γ, η, λ and N.

4.2. ESTIMATION OF PARAMETERS FOR THE MODEL

Once the model for the background has been designed as detailed in the previous section, the parameters pertaining to the model need to be estimated in order to achieve a close fit with the observed PDF. In order to calculate the observed PDF (based on the actual data present), the histogram of the background values at predefined uniform intervals is computed. A sample probability density function computed by way of the histogram for one of the runs in May 2003 is shown in Figure 4.2. Note that the RX statistic shown here ranges from 0.5 to 1. This is due to the transformation done as per equation 3.6. The values between 0 and 0.5 are neglected since that region of the curve is non-consequential.

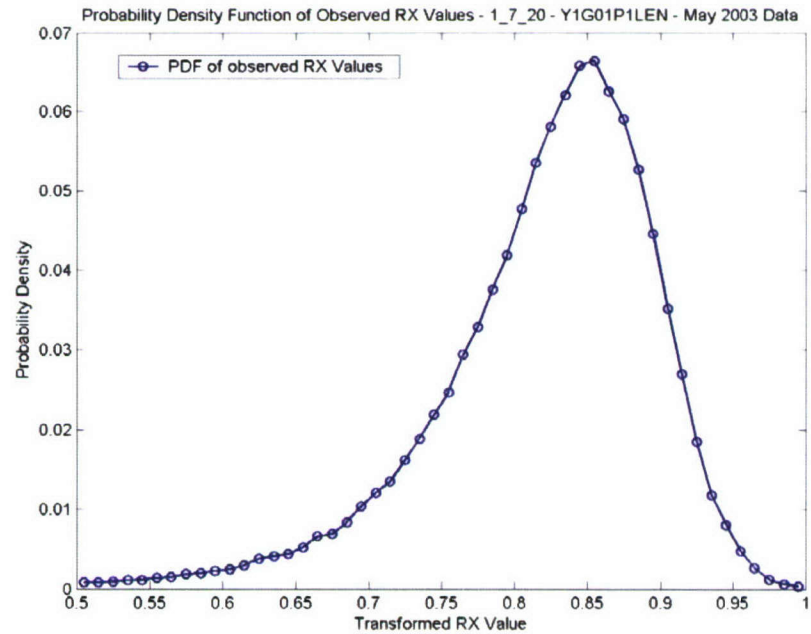

Figure 4.2. Probability Density Function of Observed Data – One Run in May 2003 Data.

Parameter estimation can be done in several ways. A simple solution would be to do a least squares minimization over an assumed sample space for the parameters. One such method called the 'prediction – error' method is used to determine the best fit parameters. A two – pass search is done in the sample space, such that the best fit parameters have fine resolution. The first pass is done using a coarse sample space to get a rough estimate of the parameters. The second pass is done using a finer resolution on the sample space, such that the best fit parameters are chosen in such a manner as to get a closely modeled distribution. The next two subsections detail the implementation of the prediction error method and the sliding window method for the parameter estimation and modeling.

4.2.1. Prediction – Error Method. The values for γ, η, λ and N can be estimated using an estimation method as described in this section. This approach is called the prediction-error method [36]. In this method, to estimate the values for the parameters, an arbitrary sample space for each of the parameters γ, η, λ and N is assumed. This sample space forms the initial search space and a brute force search is done across the sample spaces, to identify a set of values for γ, η, λ and N for the modified 3-parameter beta PDF that is at a minimum distance from the measured PDF. In order to do this, for every set of γ, η, λ and N, the error between the modeled PDF and the observed PDF is calculated by taking the Euclidean distance between the two PDFs. Amongst the error values computed, the minimum error is determined. Using a reverse lookup in the respective sample spaces, the predicted values of γ, η, λ and N are determined. After a coarse estimate of the four parameter values is done, a finer resolution sample space around the coarse samples is assumed and the prediction error method is reiterated. This second-pass results in finer resolution on the estimated parameters and thus a better fit. The method can be diagrammatically explained as shown in Figure 4.3. The block diagram in Figure 4.3 shows the schematic for the general prediction – error method which estimates parameters $p_1^*, p_2^* \ldots p_Q^*$. Thus a Q dimensional sample space is formed and a reverse lookup done to estimate the parameters. In the case of the problem at hand, $\gamma^*, \eta^*, \lambda^*$ and N^* are estimated for background statistics.

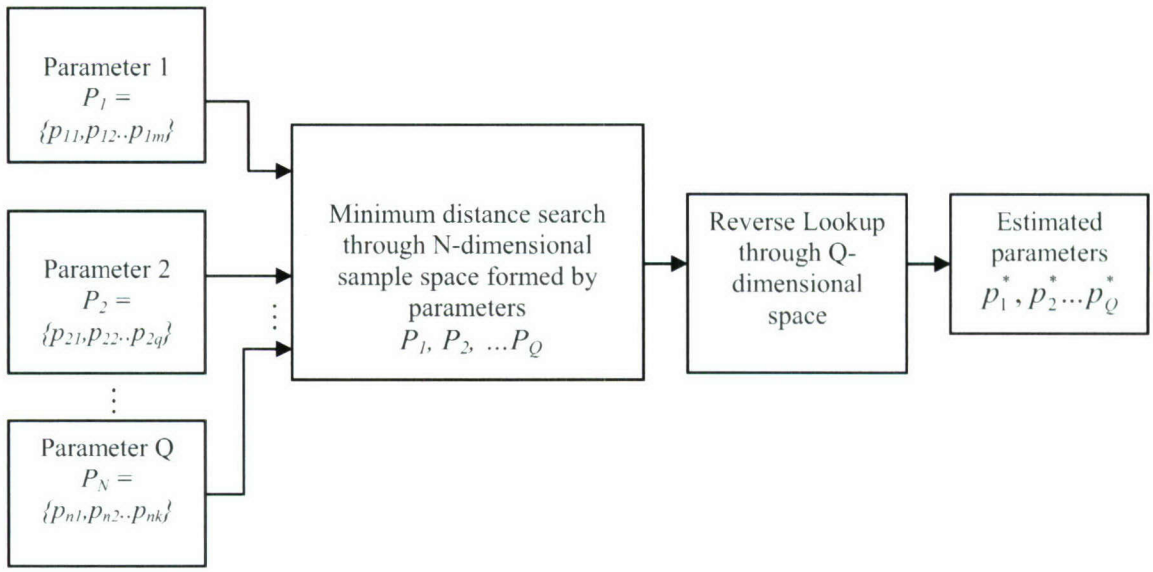

Figure 4.3. Block Diagram for the Prediction – Error Method.

4.2.2. Sliding Window Implementation. The distribution that is formed with the help of the prediction error method is a close fit to the observed distribution. The terrain that is encountered in the images at hand typically varies, within runs. The resulting PDF for the whole data will tend to be more and more Gaussian as per the central limit theorem. Thus, the parameters of the generalized beta PDF that are calculated over the whole run cannot be taken as an indicator of the behavior of the data. In order to overcome this problem, the parameters are estimated over a smaller subset of images. This is done with the help of a setup shown in Figure 4.4. Within the length of one run, starting from the first frame, p (= 2 in Figure 4.4) frames on either side of the current frame are chosen and the modeling is done on them. Similarly, a smaller subset of files are chosen by selecting q (= 1 in Figure 4.4) frames ($q < p$) on either side of the current frame for mapping of anomaly detector values for algorithmic fusion explained in Section 4.2.3. This window is then moved by $2*q + 1$ frames, and the process is repeated. Since $q < p$, there is a small overlap between the modeled frames. The overlap allows for a continuity in the estimates of the parameters of the model over each window. The next subsection explains in detail, the mapping of anomaly detector values from the original basis to a common basis in order to facilitate comparison.

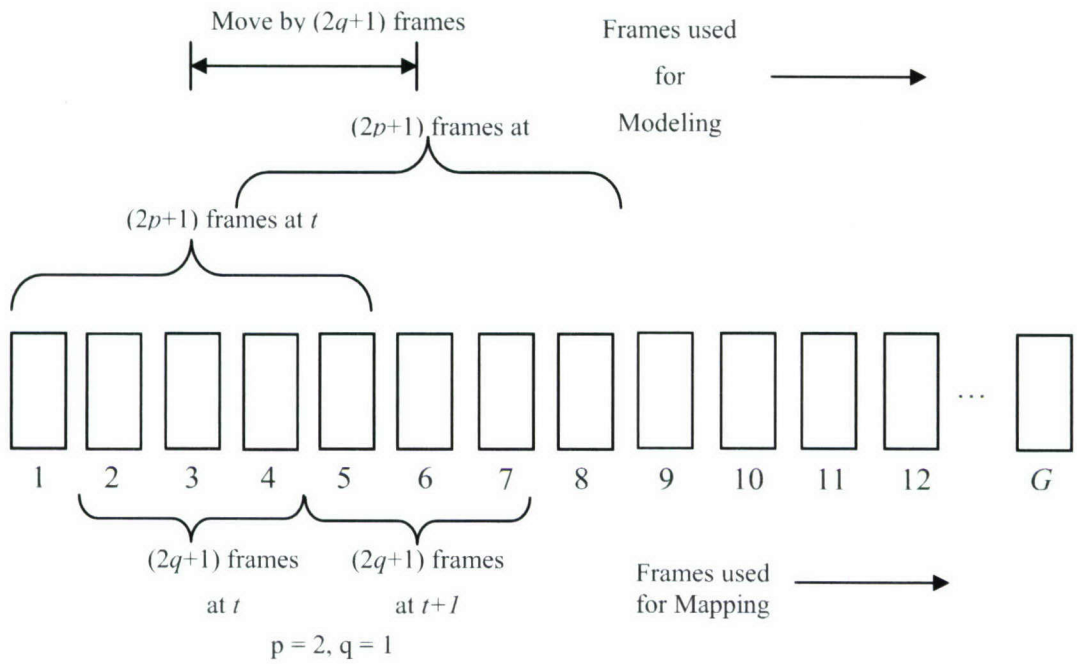

Figure 4.4. Sliding Window Implementation for Modeling and Remapping.

4.2.3. Mapping of Anomaly Detector Values. Detection statistics should have a common basis to facilitate comparison. One way to create a common basis is to map detection statistics onto a common probability distribution for a common algorithm. But the primary disadvantage of this method of mapping is that the parameter / algorithm, to which the other parameter sets / algorithms are mapped to, should be available beforehand. This is often not possible, especially in linear single path systems like the LAMDFAM GUI [37], where the general flow is to process only one parameter (or one algorithm) at any given time. In order to avoid this problem, an alternate solution would be to map all the values from all parameter/algorithm sets to a common probability distribution. Choices for this generic distribution could be any valid probability distribution, like the uniform distribution, or even the standard beta distribution. One problem with using the uniform distribution is that since the amplitude of a uniform distribution is constant. The output mapped values dramatically increase for the high contrast features and do not make much physical sense when compared to the original signal to clutter estimates obtained from the anomaly detectors, although the distribution

of values still makes sense. In order to avoid this technicality, a generic beta distribution with predetermined values for γ and η is selected and the mapping is done onto the 3 parameter beta distribution developed in Section 4.1. The mapping is represented as:

$$x = \mathrm{B}^{-1}_{\gamma,\eta,N}(F_3(x;\gamma,\eta,\lambda,N)) \tag{4.3}$$

where $\mathrm{B}_{\gamma,\eta,N}$ represents the cumulative distribution function of the modified standard beta distribution (including the effect of non-max), x is the mapped anomaly detector statistic and $F_3(x;\gamma,\eta,\lambda,N)$ represents the cumulative distribution function of the modified 3 parameter beta distribution shown in equation 4.2.

4.3. MODELING RESULTS FOR SIMULATED DATA

In order to validate the model developed so far, the modeling algorithm is tested for simulated images. The simulated images contain embedded mine-size target signatures placed in different uncorrelated and correlated additive noise. The simulated images take on dimensions of 300 x 2000 and mine-like simulated targets of various sizes (radii of 1, 2 and 3) are placed at regular intervals (50 pixels apart) in order to mirror a patterned minefield. The mean gray values of the targets are chosen in a random manner from a pre-specified range of values (1.25 ~ 2.5). In order to simulate the background, normally distributed noise with a variance of '1' is added. An example of a simulated image for uncorrelated background is shown in Figure 4.5.

Figure 4.5. Simulated Image (300 x 2000) Showing Targets.

In order to get a better estimate of the performance of the modeling scheme, a Monte-Carlo simulation [38] is done, i.e. M images are generated in a random manner by adding random noise for the background and also picking random values for the mine signatures within a predetermined range. The modeling scheme is run for all the M images together such that the performance is measured over M images instead of 1 synthesized image.

Results are simulated for uncorrelated noise and two different correlation lengths for a Gaussian spatial correlated function. The following subsections explain these results in detail.

4.3.1. Analysis for Uncorrelated Background. In this section, the Monte Carlo simulated images are designed in such a manner that the background noise that is added is uncorrelated. This condition satisfies the assumption made by Reed and Yu [22]. In the case of uncorrelated background, the data that is given as input to the RX anomaly detector is assumed to be Gaussian distributed as $N(\mu,\sigma^2 I)$ where I is the identity matrix signifying that the data is uncorrelated. Modeling results for the simulated uncorrelated data are generated for a specific non-max block size of 8. As explained earlier, the block size for non-max suppression is the radius under which the local maximum is considered to have been detected.

Due to the uncorrelated nature of the background, the targets are detected very well. Figure 4.6 shows the probability distributions under uncorrelated noise. Figure 4.6 (a) shows the results of parameter estimation for 50 uncorrelated background simulated images, for target radius 1. Figures 4.6 (b) and (c) show the same for target radii 2 and 3. The figures show the observed and modeled density distributions under null hypothesis. From these figures, it is seen that under uncorrelated noise, the observed PDF is almost perfectly modeled by the modeled PDF. The only difference between the three plots is the spread of values, or the width of the probability distribution. On the plots, the green hexagram mark on the *x-axis* shows the mean value for detection statistics. As expected, the mean value of the RX detection statistics decreases with increasing target radius. Similar probability distribution fits are performed for correlated background correlated by a Gaussian correlation function with different correlation lengths in the following subsections.

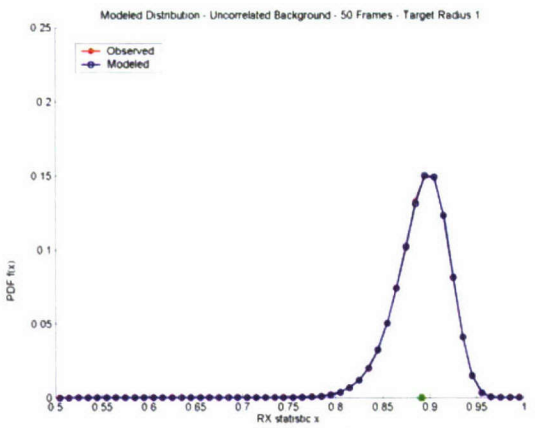

(a) Target Radius 1

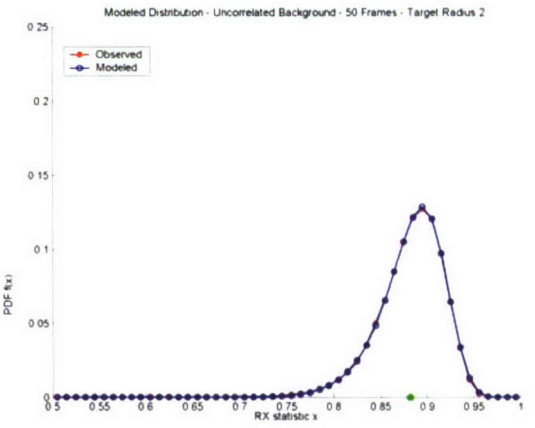

(b) Target Radius 2

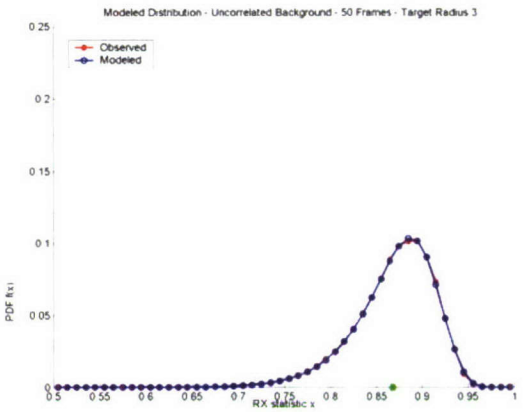

(c) Target Radius 3

Figure 4.6. Probability Distributions for Uncorrelated Noise.

The estimated values of γ, η, λ and N are tabulated as in Table 4.1. Since the parameters are four in number, identifying trends in the parameter variations becomes difficult. One observation that can be made from the parameter variations shown in Table 4.1 is that, the sample space that is allocated for the modeling algorithm to search for the minimal error has to be adjusted for each set of parameters in order to provide freedom for the search algorithm to settle down to values that are reasonably within the limits of the search space. Another point to note is that η is almost constant while γ decreases with target radius. In the next section, the analysis for the same kind of simulated images but with correlated background is presented and compared to uncorrelated background presented here.

Table 4.1. Estimated Values of Model Parameters for Uncorrelated Noise.

	γ	η	λ	N
Target Radius 1	94.4	13.9	0.891	0.95
Target Radius 2	26.6	14	0.271	1
Target Radius 3	13.4	15	0.136	0.6

4.3.2. Analysis for Correlated Background. The simulated data in this section is designed in such a manner that the background is correlated with a correlation function Λ. The purpose of introducing correlation in the simulated image background is that this situation is closer to real life imagery. Real world imagery is seldom uncorrelated. The amount of correlation varies according to background terrain. Thus introducing correlation into the simulated data should give an approximate indication of the performance of the modeling algorithm for real world data. Figures 4.7 shows the Gaussian correlation functions used with correlation lengths of 0.4 (Figure 4.7 (a)) and 0.6 (Figure 4.7 (b)), respectively.

(a) $\sigma_s = 0.4$ (b) $\sigma_s = 0.6$

Figure 4.7. Gaussian Correlation Function.

Figure 4.8 shows the results of the modeling process for the correlated backgrounds with correlation length of $\sigma_s = 0.4$. Due to the introduction of correlation, the PDF are biased towards the higher end as compared to the uncorrelated case

indicating a higher likelihood of false alarms for a given RX statistic (signal to clutter ratio). This is because, with the introduction of correlation for the background pixels, the probability of local regions of the background being statistically similar to a mine target becomes higher, thus introducing more false alarms than the uncorrelated case.

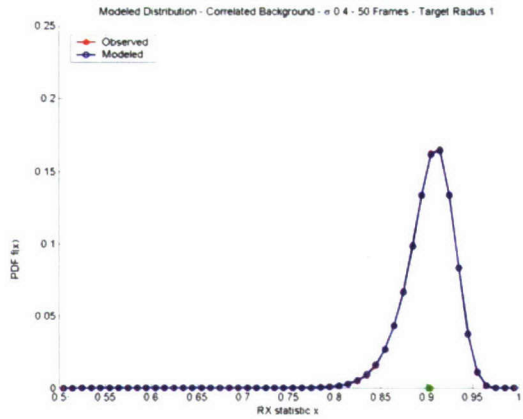

(a) Target radius 1

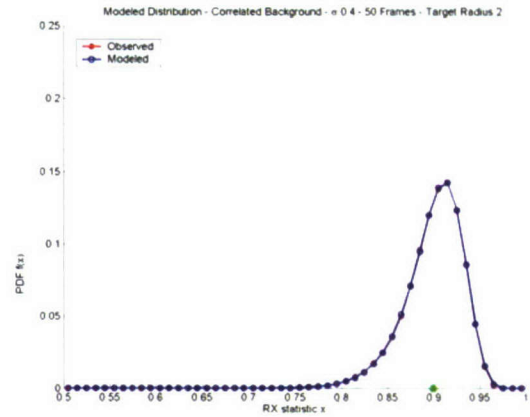

(b) Target radius 2

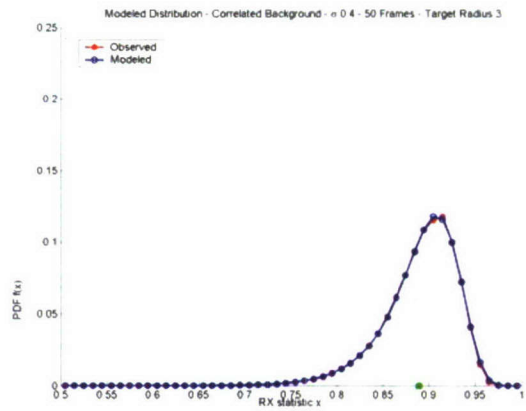

(c) Target radius 3

Figure 4.8. Probability Distributions for Correlated Noise $\sigma_s = 0.4$.

Similar to the uncorrelated case, a tabulation of the estimated parameters for the model are given in Table 4.2. The variation in the parameters noticed here is quite similar to the ones seen for the uncorrelated case in Table 4.1.

Table 4.2. Estimated Values of Model Parameters for Correlated Noise - $\sigma_s = 0.4$.

	γ	η	λ	N
Target Radius 1	91.6	12.4	0.906	1.6
Target Radius 2	22.6	13	0.211	1.15
Target Radius 3	12.4	12	0.136	1.1

A similar procedure is adopted for simulating a correlated background with $\sigma_s = 0.6$. Table 4.3 shows the estimated values of the parameters of the model for the correlated background with $\sigma_s = 0.6$. The values of γ and λ are much lower than the other cases found in Tables 4.1 and 4.2.

Figure 4.9 shows the modeling curves for the target radii 1, 2 and 3 like the earlier cases. It is seen that the mean of the modeled probability density function moves closer to 1 as the correlation length σ_s increases. Because of this, it is seen that the mean values of the PDFs are higher and as explained before the detection response is expected to give higher false alarms than before.

Table 4.3. Estimated Values of Model Parameters for Correlated Noise - $\sigma_s = 0.6$.

	γ	η	λ	N
Target Radius 1	23.6	14.8	0.106	0.65
Target Radius 2	11.2	13.3	0.051	1.1
Target Radius 3	5.6	9.9	0.041	2.1

4.4. MODELING RESULTS FOR AIRBORNE DATA

The airborne landmine data described in Section 2 can be modeled using the modeling algorithm presented in this chapter. Because of the sliding window method of parameter estimation explained in Section 4.2.2, the results of modeling cannot be shown in the form of the curve fits shown for simulated data in the previous section. Instead, the

effect of modeling can be explained in the following two subsections with the help of different types of plots and tabulations. The runs considered in this section do not have any mines in them. Figures 4.10 – 4.13 show representative sample images for each of the different environment considered. These images give a preliminary idea of the characteristics of the images for different backgrounds and times of the day. The results of modeling are discussed in the subsequent subsections.

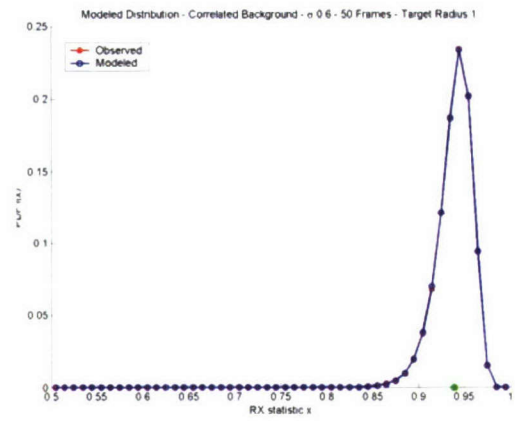

(a) Target radius

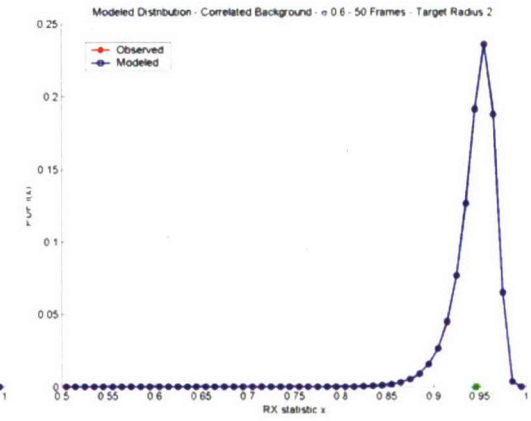

(b) Target radius 2

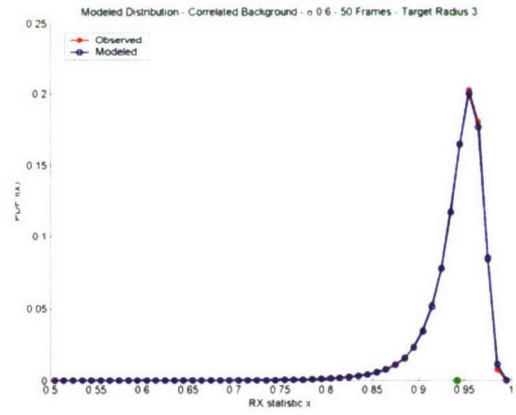

(c) Target radius 3

Figure 4.9. Probability Distributions for Correlated Noise $\sigma_s = 0.6$.

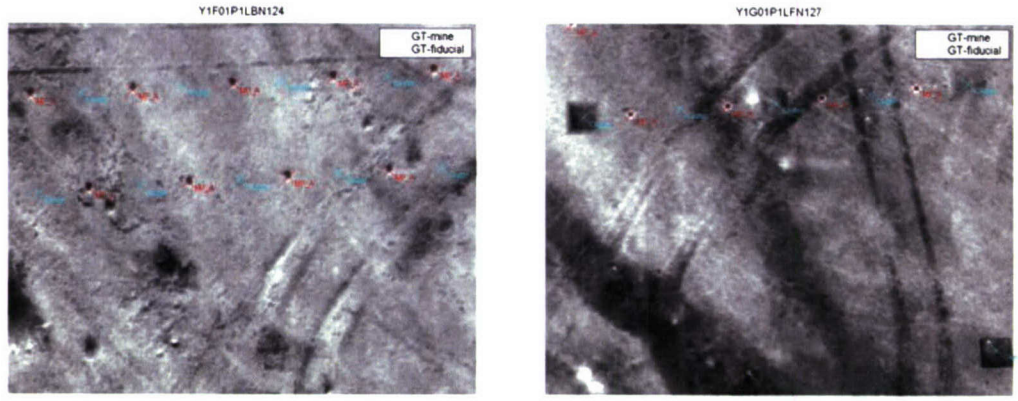

(a) Daytime (b) Nighttime

Figure 4.10. Sample Images Showing Mine Area.

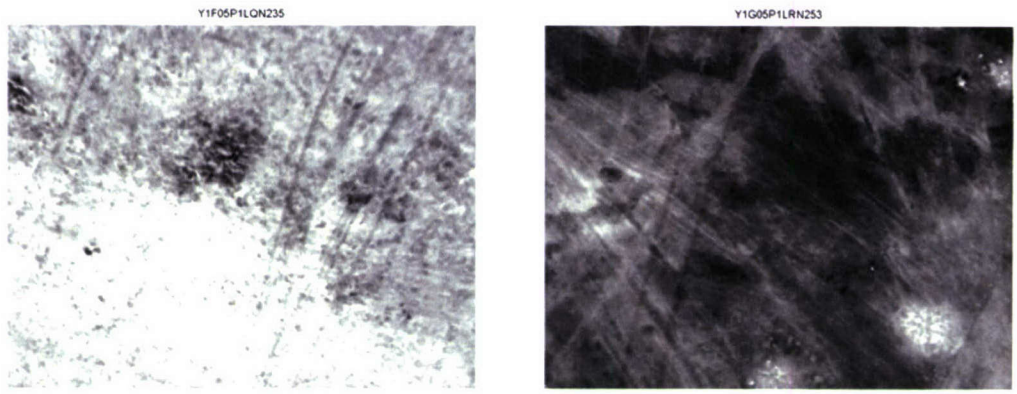

(a) Daytime (b) Nighttime

Figure 4.11. Sample Images Showing Wash 05 Terrain.

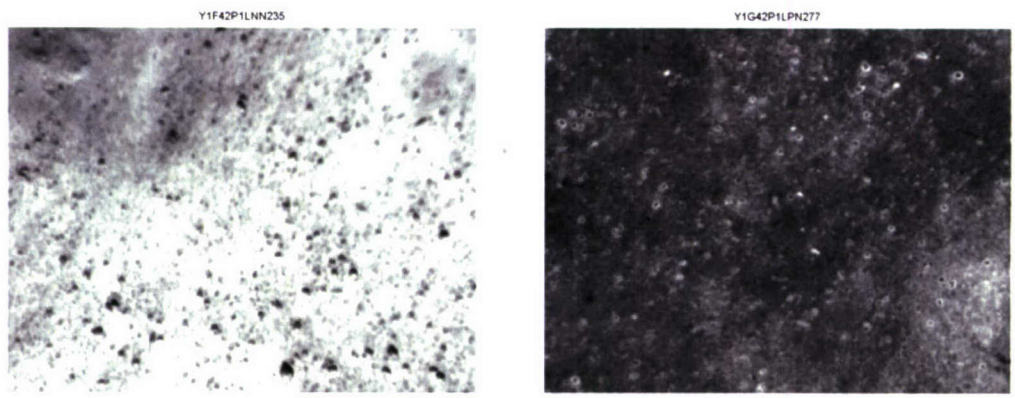

(a) Daytime (b) Nighttime

Figure 4.12. Sample Images Showing Rock 42 Terrain.

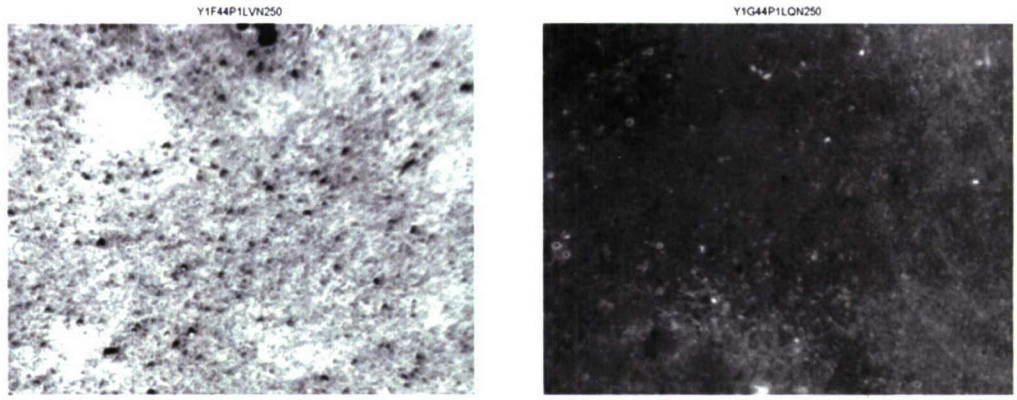

(a) Daytime (b) Nighttime

Figure 4.13. Sample Images Showing Rock 44 Terrain.

4.4.1. Variation of RX Threshold With Time. A method of effectively conveying the impact of modeling the data would be to observe the change in the RX threshold across different windows in a run for a fixed false alarm rate. The RX threshold value is the minimum value of the RX statistic at which a particular false alarm rate is achieved. This is equivalent to observing the variation of the RX threshold with time. The RX values presented here are the original values before remapping. Ideally the RX threshold across a run is expected to be almost constant. But as a result of the inherent inhomogeneities of the data even across the same run, there are significant variations in the estimated RX threshold.

The following figures (Figures 4.14 – 4.17) show the estimated RX threshold for different frames over a run for different terrain for daytime images. The three different false alarm rates used are 0.1, 0.01 and 0.001.

In the following figures, the subplot section (a) shows the variation of the RX threshold with time and the subplot (b) shows the shape of a typical PDF found in the terrain which (a) specifies in the region circled on (a). In Figures 4.14 (a) and 4.15 (a) it is seen that the variation in the RX threshold for mine area and the Wash 05 terrain is quite similar and is over a smaller range of values. From Figures 4.16 (a) and 4.17 (a) it is seen that for the rocky terrain, the variation is RX threshold is similar to each other but large compared to the mine area and Wash 05.

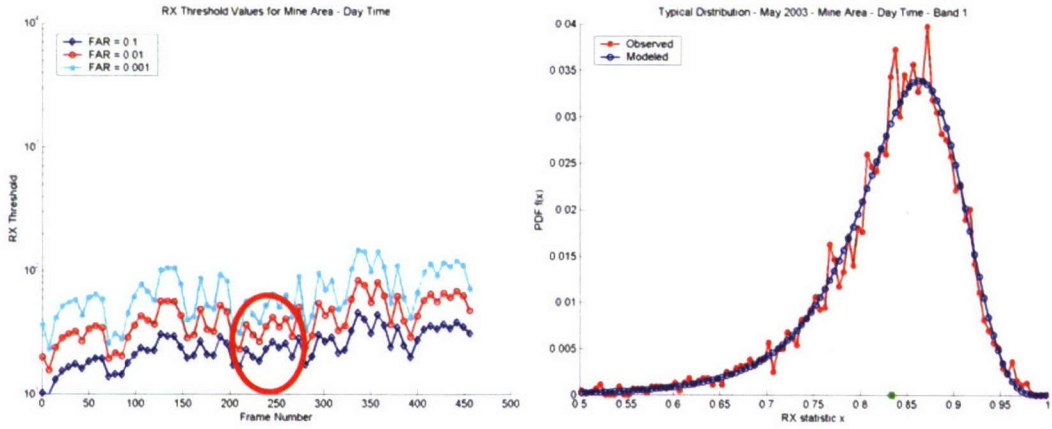

(a) RX Threshold Variation (b) Typical Distribution

Figure 4.14. Mine Area - Daytime – $\gamma = 12.5,\ \eta = 5.7,\ \lambda = 0.59,\ N = 2.4$.

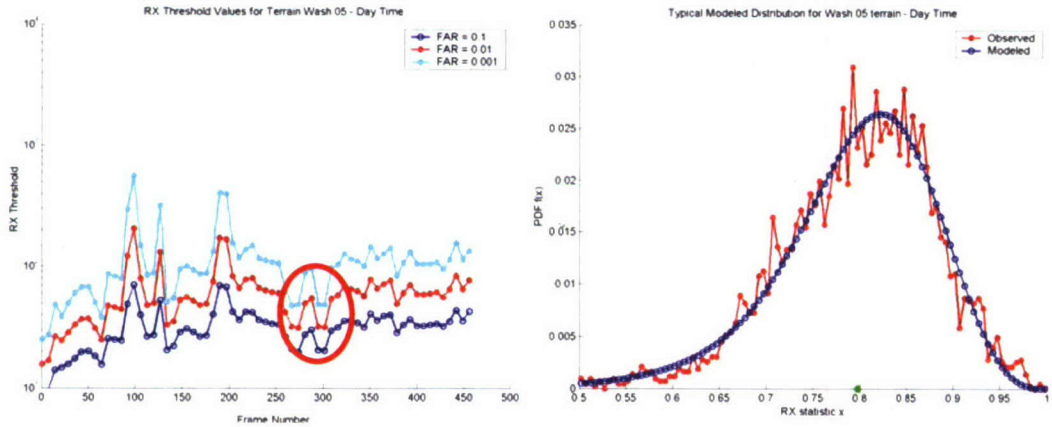

(a) RX Threshold Variation (b) Typical Distribution

Figure 4.15. Wash 05 Terrain - Daytime – $\gamma = 12.5,\ \eta = 4.1,\ \lambda = 1.4,\ N = 4$.

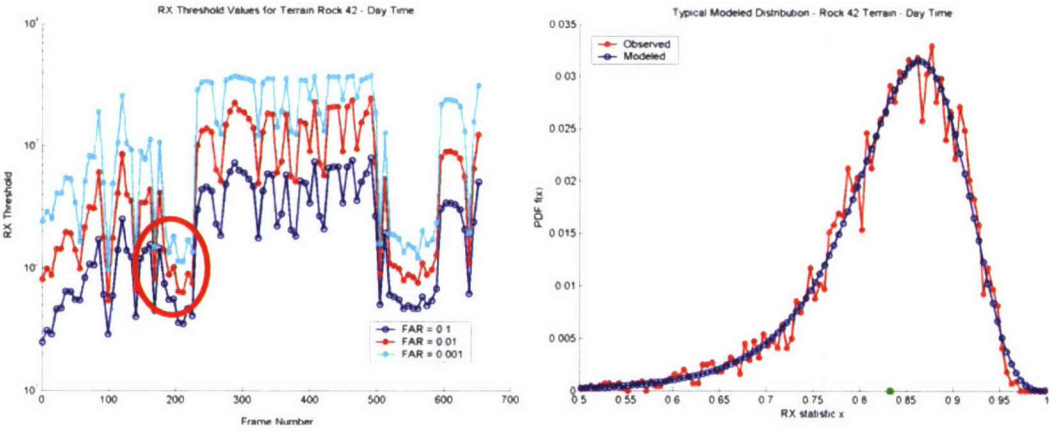

(a) RX Threshold Variation (b) Typical Distribution

Figure 4.16. Rock 42 Terrain - Daytime – $\gamma = 9.3,\ \eta = 4.5,\ \lambda = 0.6510,\ N = 3.2$.

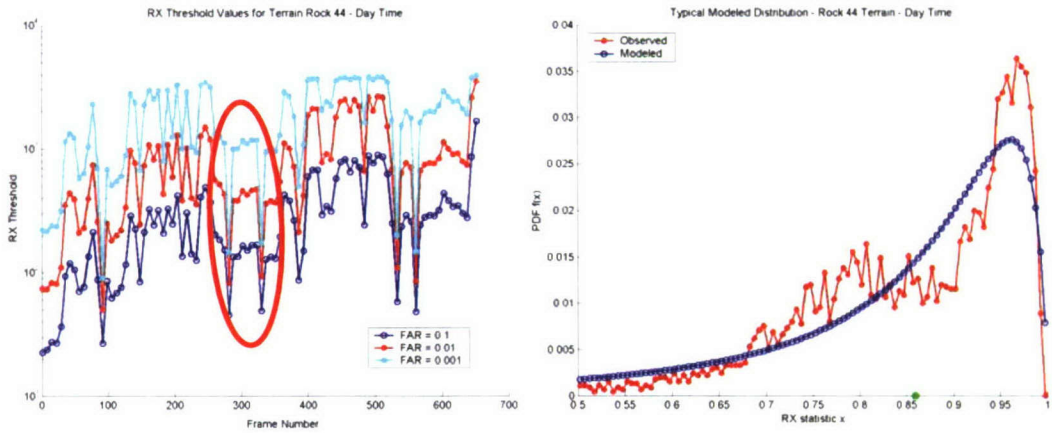

(a) RX Threshold Variation (b) Typical Distribution

Figure 4.17. Rock 44 Terrain - Daytime – $\gamma = 0.1$, $\eta = 1.7$, $\lambda = 0.0910$, $N = 9.6$.

Figures 4.18 – 4.21 show similar variations in the RX threshold for nighttime images across different frames over a run for different terrain. Similar to the daytime data, the RX threshold variation for the mine area and Wash 05 terrain are quite similar and lower in the range of variation. The rocky terrains are similar to each other as well, with higher variation in the RX threshold compared to the mine area and wash terrain. The overall range of values of the RX threshold for the nighttime data is lower as compared to the daytime data.

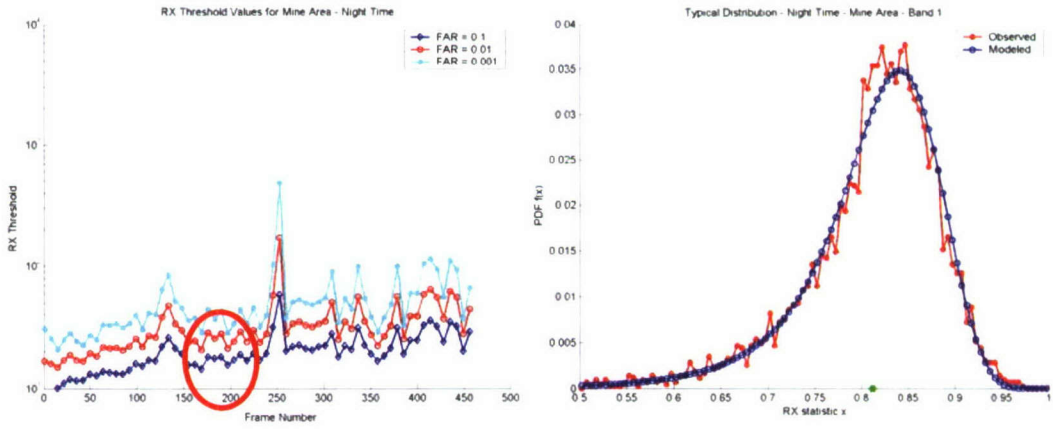

(a) RX Threshold Variation (b) Typical Distribution

Figure 4.18. Mine Area - Nighttime – $\gamma = 5.7$, $\eta = 10.1$, $\lambda = 0.1810$, $N = 3.2$.

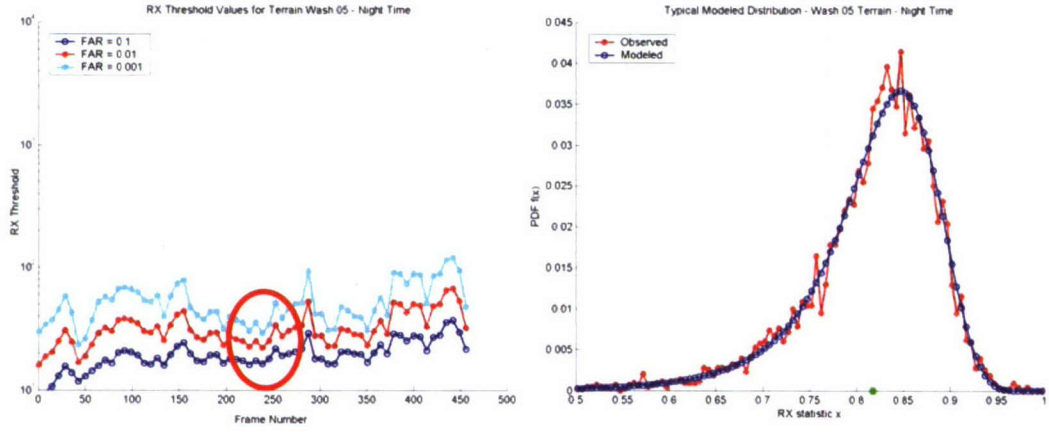

(a) RX Threshold Variation (b) Typical Distribution

Figure 4.19. Wash 05 Terrain - Nighttime – $\gamma = 6.1$, $\eta = 11.7$, $\lambda = 0.1510$, $N = 2.8$.

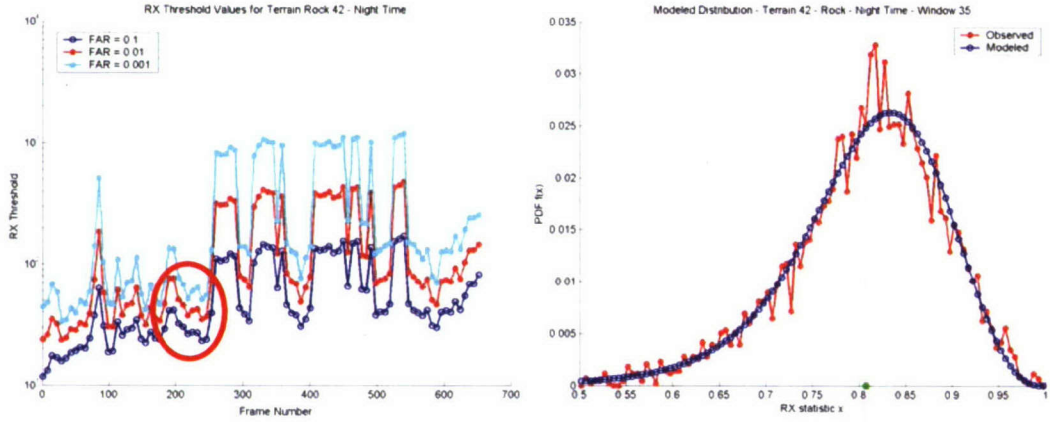

(a) RX Threshold Variation (b) Typical Distribution

Figure 4.20. Rock 42 Terrain - Nighttime – $\gamma = 7.1$, $\eta = 7.3$, $\lambda = 0.23$, $N = 1$.

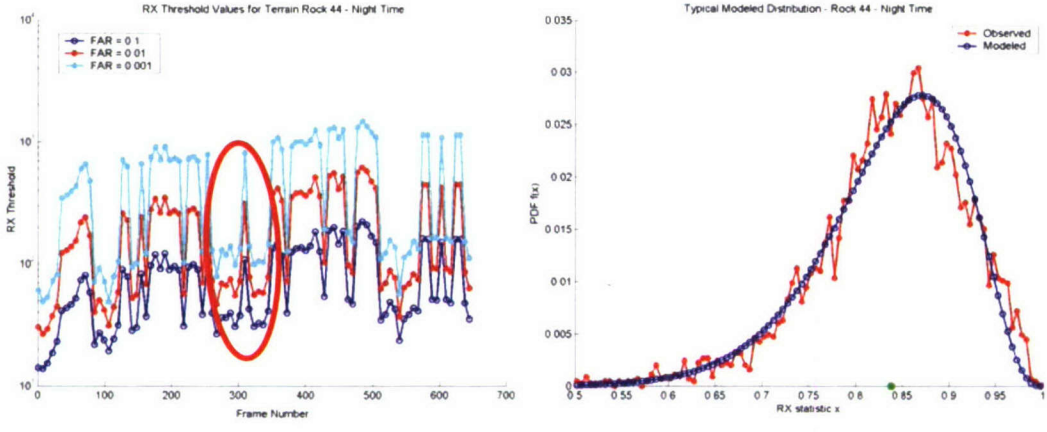

(a) RX Threshold Variation (b) Typical Distribution

Figure 4.21. Rock 44 Terrain - Nighttime – $\gamma = 12.9$, $\eta = 4.1$, $\lambda = 0.6010$, $N = 0$.

It can be observed from the plots that as the inhomogeneity in the data increases, the variation in the RX threshold with respect to time increases. As expected, the variation in the mine area is much lower than the variation in the rocky terrain. This difference in the variation also provides an indicator of the likelihood of detection of mines in these different terrain. The expected behavior of the plots shown is that, the variation in the RX threshold should be almost constant. From the plots shown, it can be observed that the expected behavior of the RX threshold is not satisfied in a lot of cases, especially the terrains that have high inhomogeneities in them. As the false alarm rate increases, the RX threshold value increases. It can be seen that the RX value for a given FAR changes significantly with time. Figure 4.22 shows the variations of the RX threshold across one run from the Rock 42 nighttime data for three different false alarm rates. In order to explain these spikes, specific PDF behavior for particular windows is displayed and the reason for such errant behavior explained.

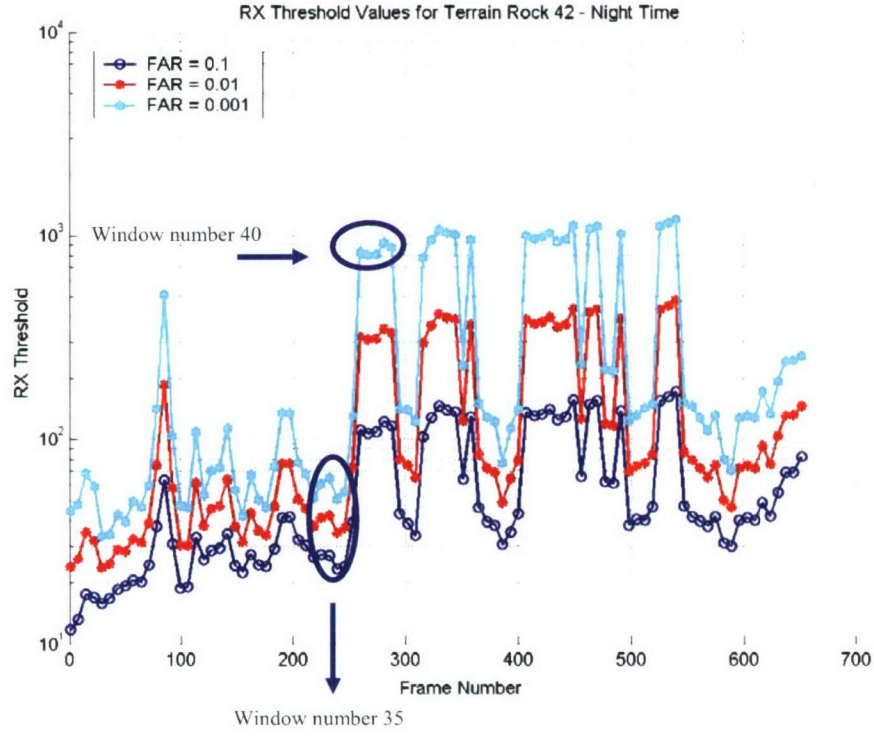

Figure 4.22. Variation in RX Threshold - Different Windows for Rock 42 – Nighttime.

Figures 4.23 and 4.25 show specific image frames from windows 35 (frames 234 – 244) and 40 (frames 269 – 279), respectively from the run, *Y1G42P1LPN*. The colored boxes on the images are the most prominent thresholded RX detections. Figures 4.22 and 4.24 show the respective probability density function fits for windows 35 and 40.

As can be seen from the probability density function fits, the model of window 35 has more points near 0.9 ~ 1.0 and so that part of the curve is smoother. But in the case of the model of window 40, the tail of the distribution is very sharp. This means that there are not too many points in the higher end of the statistic value range and because of this, earlier bins in the plot get more values assigned to them. This is a clear sign of high false alarms and in order to detect these false alarms at the constant rate stipulated, the RX threshold has to be very high compared to a model that has a gradually declining slope. This is the reason for high peaks noticed in Figure 4.22.

In addition to presenting the plots on RX threshold variations, the mean RX threshold value for different fixed false alarm rates are tabulated in Tables 4.4 and 4.5 for both day and nighttime images for different terrain. These tables can be used to compare the mean RX value required to achieve the specified false alarm rate. Table 4.4 shows that the Rock 42 and Rock 44 runs require a higher mean threshold on the RX statistic to achieve the false alarm rate shown. Lower threshold denotes more homogeneity in the background and thus better detection if mines are placed in such backgrounds.

Table 4.5 shows a similar table for nighttime data. A similar performance trend is shown by the three terrain to daytime but the relative threshold values are lesser than daytime.

4.4.2. Variation of RX Threshold with False Alarm Rate. Another method of displaying the effect of modeling would be to show the variation of the mapped RX threshold value with reference to the false alarm rate (FAR). The RX thresholds required for different false alarm rates across different backgrounds are compared on a logarithmic scale. The false alarm rate is computed per square meter. Figure 4.27 shows the plot of the RX threshold against false alarm rate for four different backgrounds collected during daytime from the May 2003 data collection.

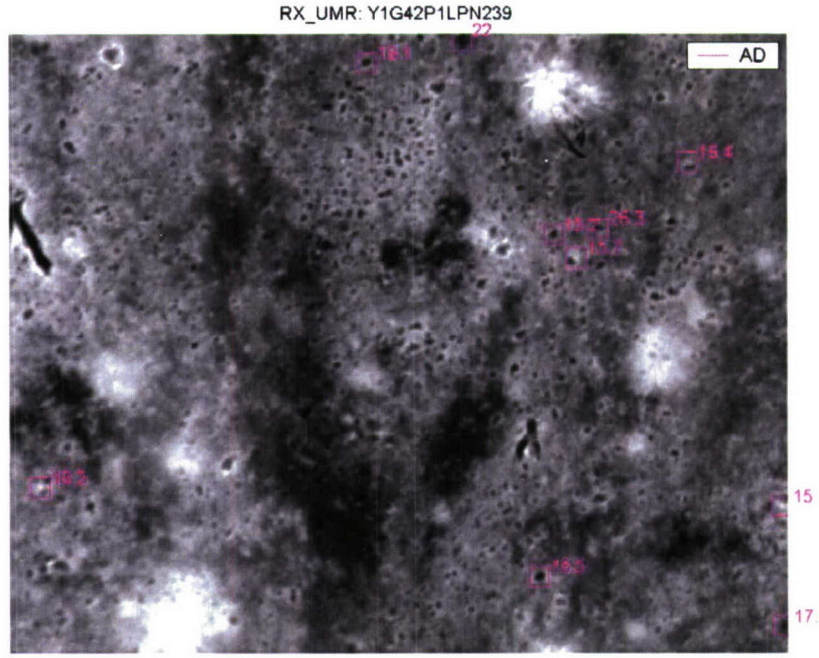

Figure 4.23. Raw Image Y1G42P1LPN239 From Window 35 (Frame 239).

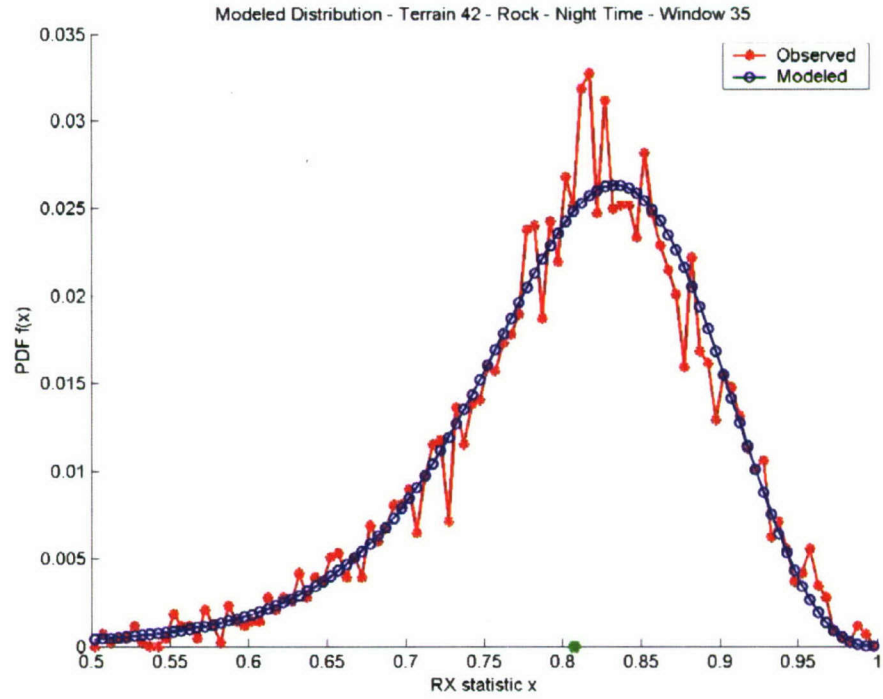

Figure 4.24. Modeled Distribution For Window 35 for Rock 42 – Nighttime Data.

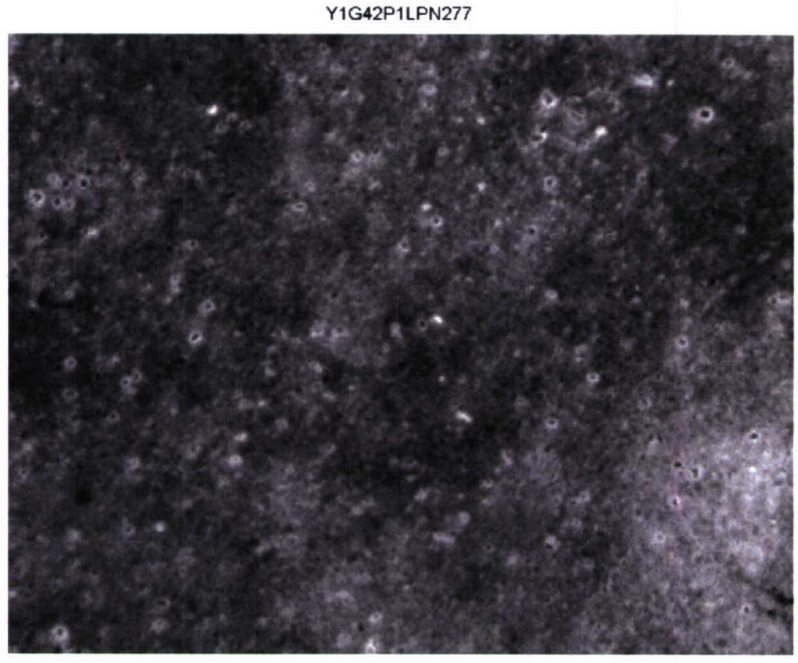

Figure 4.25. Raw Image Y1G42P1LPN277 From Window 40 (Frame 277).

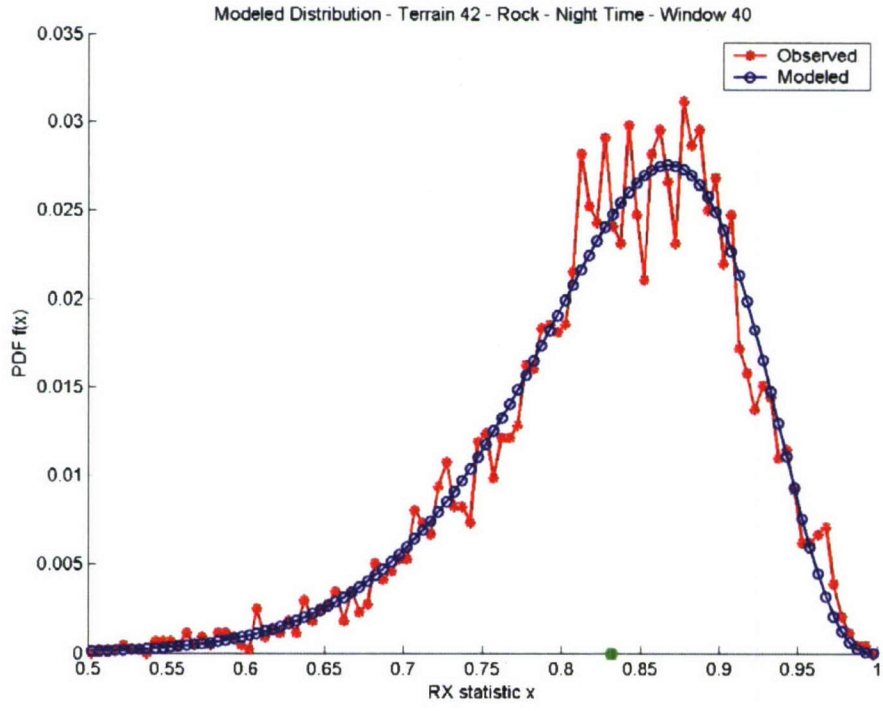

Figure 4.26. Modeled Distribution For Window 40 For Rock 42 – Nighttime Data.

Table 4.4. RX Threshold Values for Various Terrain for Daytime Data.

		False Alarm Rate (FA / sq.m)		
		0.1	0.01	0.001
Mean RX Threshold	Mine Area	25	42	70
	Wash 05	32	61	117
	Rock 42	259	754	1633
	Rock 44	303	865	1875

Table 4.5. RX Threshold Values for Various Terrain for Nighttime Data.

		False Alarm Rate (FA / sq.m)		
		0.1	0.01	0.001
Mean RX Threshold	Mine Area	20	34	56
	Wash 05	20	33	53
	Rock 42	61	145	336
	Rock 44	79	206	504

Figure 4.27 (a) shows the minimum RX threshold (before remapping) required to achieve a given FAR for each type of background. It should be noted that these are aggregate results computed over all frames for a given run (455 or 650 as the case maybe). As discussed earlier, the RX threshold may vary significantly with time. A high value for the RX threshold at a given FAR implies that there is a large prevalence of high contrast anomalies in the background. From Figure 4.27 (a), it is observed that for a given FAR, the backgrounds Rock 42 and Rock 44 require a higher threshold compared to Wash 5 and the Mine Area 1. Equivalently, Rock 42 and Rock 44 would result into a higher FAR for a given RX threshold (minimum contrast measure) as compared to Wash 5 and mine area.

Figure 4.27 (b) shows the same plot after remapping the RX statistics. The remapped RX thresholds for each of the backgrounds are plotted on a log scale against corresponding false alarm rates. The corresponding plot for the standard beta variate

distribution is also shown. The FAR value is shown out to an FAR of 1, which corresponds to approximately 250 false alarms per image frame. In the high FAR region of 10^{-1} to 10^{0} (corresponding to 25 – 250 targets per image frame), the plots for all the background types converge to the plot for the beta variate. This is expected due to the remapping operation which makes the RX statistics CFAR across different backgrounds. However we note that there is significant difference between different backgrounds in the low FAR region of 10^{-4} to 10^{-2}. A heavier tail of the mapped CDFs would mean that the terrain is harder to detect and would correspond to the performance of Wash 5 and the Mine Area 1. A lighter tail for the same would signify that the terrain is easier to detect than the standard beta density and would correspond to the performance of Rock 42 and Rock 44. If the terrain lies above the standard beta distribution curve, it implies that the background has a higher density of high contrast anomaly targets than would be dictated by the standard beta distribution. In this particular figure, it is seen that Rock 42 and Rock 44 lie below the standard beta plot and Wash 5 and Mine Area 1 lie above. This does not however necessarily mean that Rock 44 or Rock 42 are easier terrain for landmine detection. As noted in Figure 4.27 (a), a mine in Rock 42 and Rock 44 background requires higher signal to clutter contrast (RX value) as compared to Wash 5 and Mine Area 1.

In terms of the anomaly detector, the region of interest would be an FAR in the range of $2\text{x}10^{-2}$ to 10^{-1}. The target detected at this RX threshold region would be applied to a false alarm mitigation (FAM) scheme which is likely to follow the anomaly detector stage as shown in the block diagram in Figure 3.1. As is seen from Figure 4.27 (b), in this region, all the backgrounds almost converge to about the same RX thresholds, thus making the remapped RX statistics CFAR. Thus, if an FAM scheme is applied in succession to the RX detector, then the RX threshold chosen in this region for a particular FAR would be about the same for all the backgrounds.

Figure 4.28 presents a similar plot for nighttime data with Figure 4.28 (a) showing the original RX statistic threshold variation with FAR and 4.28 (b) showing the remapped statistic variation with FAR. The effect of this choice is seen in the dip of the plots for original RX statistics in Figure 4.28 (a) around an FAR of about $5 \text{ x } 10^{-2}$.

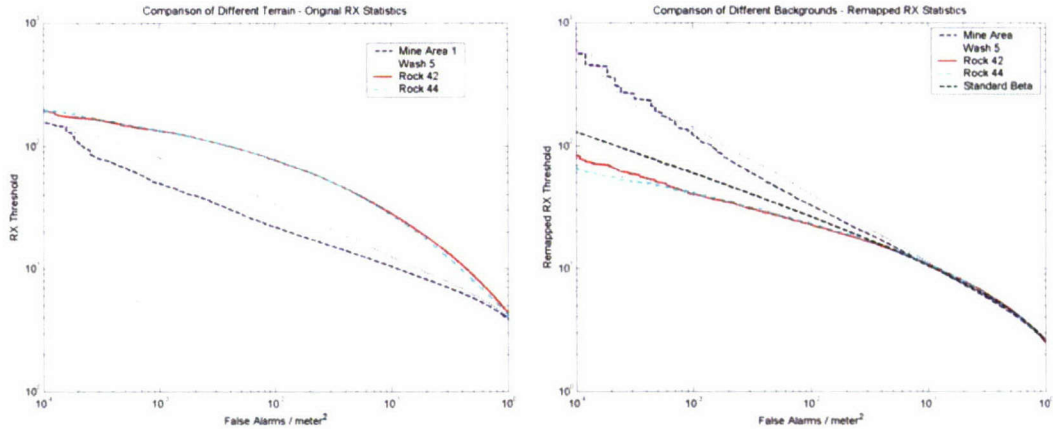

(a) Original RX statistics (b) Mapped RX statistics

Figure 4.27. Comparison of Different Terrain – May 2003 – Daytime – 0730 – 1030.

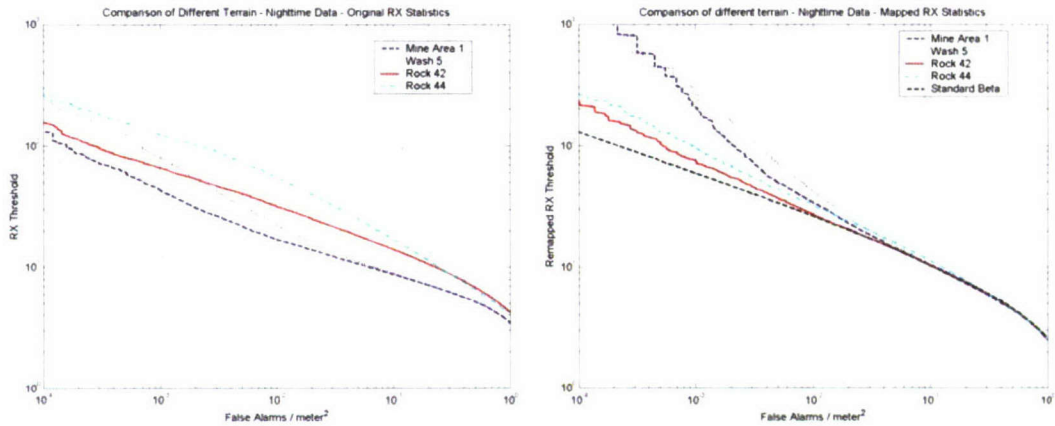

(a) Original RX statistics (b) Mapped RX statistics

Figure 4.28. Comparison of Different Terrain – May 2003 – Nighttime – 0230 – 0530.

Figures 4.29 and 4.30 show similar plots, but for more terrain and at a different time of the day. Figure 4.29 shows the variation of the RX threshold with False Alarm Rate for daytime data in the 1600 – 2000 time period for Band 0 in the May 2003 data collection. The different terrains shown include Yellow Sand 2, Wash 5, Cibola 6, Rock 41, Rock 42, Rock 43 and the Mine Area. Similar to Figures 4.27 and 4.28, these plots also have (a) and (b) subplots showing the original RX statistics and the mapped RX statistics, respectively. From Figures 4.29 and 4.30 it is apparent that the trend noticed in Figures 4.27 and 4.28 is apparent in these plots also. In terms of the original RX statistics, yellow sand 2, requires the least RX thresholds for different FAR and Wash 5 and the mine area come close to this performance. The rock backgrounds require higher RX thresholds as expected. In terms of the mapped RX statistics, similar inferences like

the ones made for Figure 4.27 (b) can be made here. Nighttime performance is quite similar to daytime performance in terms of the the behavior of the different backgrounds.

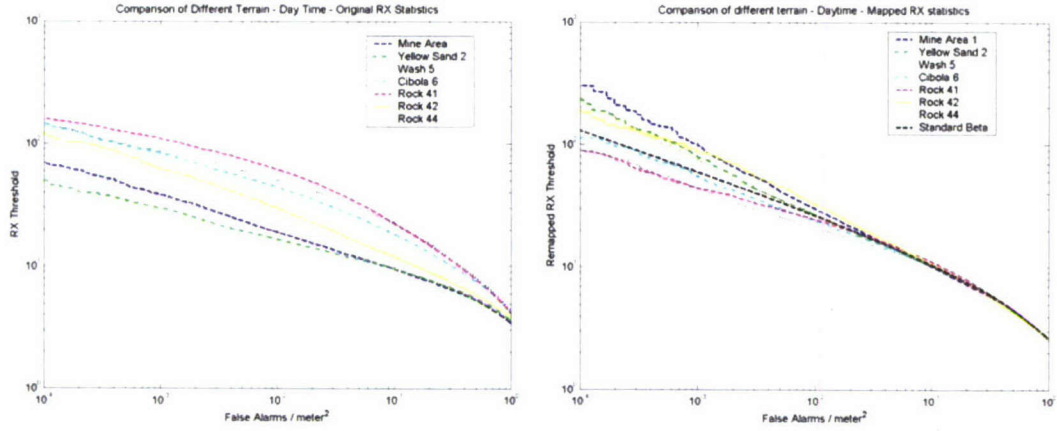

(a) Original RX statistics (b) Mapped RX statistics

Figure 4.29. Comparison of Different Terrain – May 2003 – Daytime – 1600 – 2000.

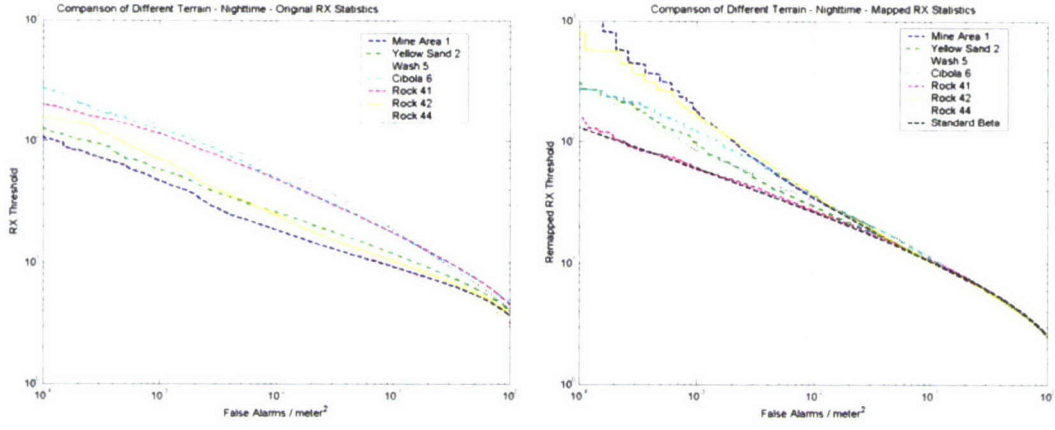

(a) Original RX statistics (b) Mapped RX statistics

Figure 4.30. Comparison of Different Terrain – May 2003 – Nighttime – 2100 – 2400.

From these plots, it is apparent that the statistics of different terrain can be readily compared. Also the mine area is probably the easiest terrain that can be used for mine detection. It is seen that background modeling is an effective tool for characterizing the different backgrounds encountered and also setting guidelines for the false alarm rates required for different backgrounds.

5. ALGORITHMIC FUSION FOR ANOMALY DETECTION

Previous analysis has shown that the performance of the RX algorithm is highly dependent upon the selected RX parameters [39]. In particular it has been shown that the target radius used in the algorithm should closely match the radius of the expected mine signature. Since the size (or any other parameter for that matter) of the expected mine signature is not known *a priori*, in such a scenario, a fusion scheme should be employed, which takes the detection statistics from each of the parameter sets and tries to make a unified decision on the likelihood of an anomaly of any size within the input range of the fusion scheme. Even though the following discussion addresses an RX based anomaly detector alone, the fusion methodology developed should be equally applicable to other anomaly detectors with different sets of parameters as applicable to the data at hand. The primary motivation is to combine outputs from different algorithms in a manner which results in a performance on par with or better than the best performing algorithm.

5.1. REVIEW OF FUSION TECHNIQUES

There are primarily three types of fusion scheme used in research and experimentation. They are: 1) Data fusion 2) Algorithmic fusion and 3) Human in the loop fusion.

5.1.1. Data Fusion or Feature Level Fusion. Data fusion primarily deals with the fusion of data from different types of sensors or data sources [40]. This type of fusion is done whenever the information gathered from any single sensor or data source is found to be insufficient. Since some suitable feature from each sensor data are used for the fusion process, this scheme is also called feature level fusion. The accuracy of the information presented to the processing algorithms is more in this case and hence better performance is expected.

5.1.2. Algorithmic Fusion or Decision Level Fusion. Algorithmic fusion is based on the fusion of multiple decision statistics. The multiple decision statistics may come from the outputs of different algorithms, different parameter selections or different sensors. Since the fusion is implemented after a decision is made based on each algorithm, it is also called decision level fusion [41]-[43].

5.1.3. Human in the Loop Fusion. Human in the loop fusion is probably one of the lesser used methods of fusion which basically relies on the ability of the human operator working at the ground station to fuse the information that is being displayed to or being gathered by the sensors [44].

5.2. ALGORITHM FUSION TECHNIQUES

Algorithm fusion can be performed using different techniques. Dobeck [41] used algorithmic fusion in the form of a simple AND operation over multiple classification algorithm outputs. A similar approach in taken by Casasent and Ye [42] where mathematical morphology based algorithm results are fused with Gabor wavelet transform based algorithm results with the help of a binary AND operation. No less than three algorithmic fusion approaches are carried out by Aridgides, Fernandez and Dobeck for the classification of sea mines in [43]. They are: logic based fusion, M-out of-N fusion and Log-likelihood Ratio (LLRT) based fusion. In this thesis, the algorithm fusion over different algorithms is done with the help of a MAX operation over all the target-lists that are obtained from the various anomaly detection algorithms.

The primary motivation behind using the max operation for fusion here is to maximize the probability of detection, since the current discussion of algorithmic fusion is aimed at anomaly detection. This is precisely what is achieved by the MAX operation as it makes the detection performance of the fused output to yield better probability of detection or performance at least on par with the best performing algorithm, even though it may correspondingly result in higher false alarm rate as well. The increase in false alarms can subsequently be reduced at the false alarm mitigation stage.

5.3. ALGORITHM FUSION FOR AIRBORNE MINEFIELD DETECTION

The algorithm fusion scheme used in this work applies to single sensor data. For the present work, instead of using multiple anomaly detector algorithms, the same anomaly detector (RX) is used with different sets of parameters. The architecture used for the fusion scheme is shown as in the block diagram in Figure 5.1.

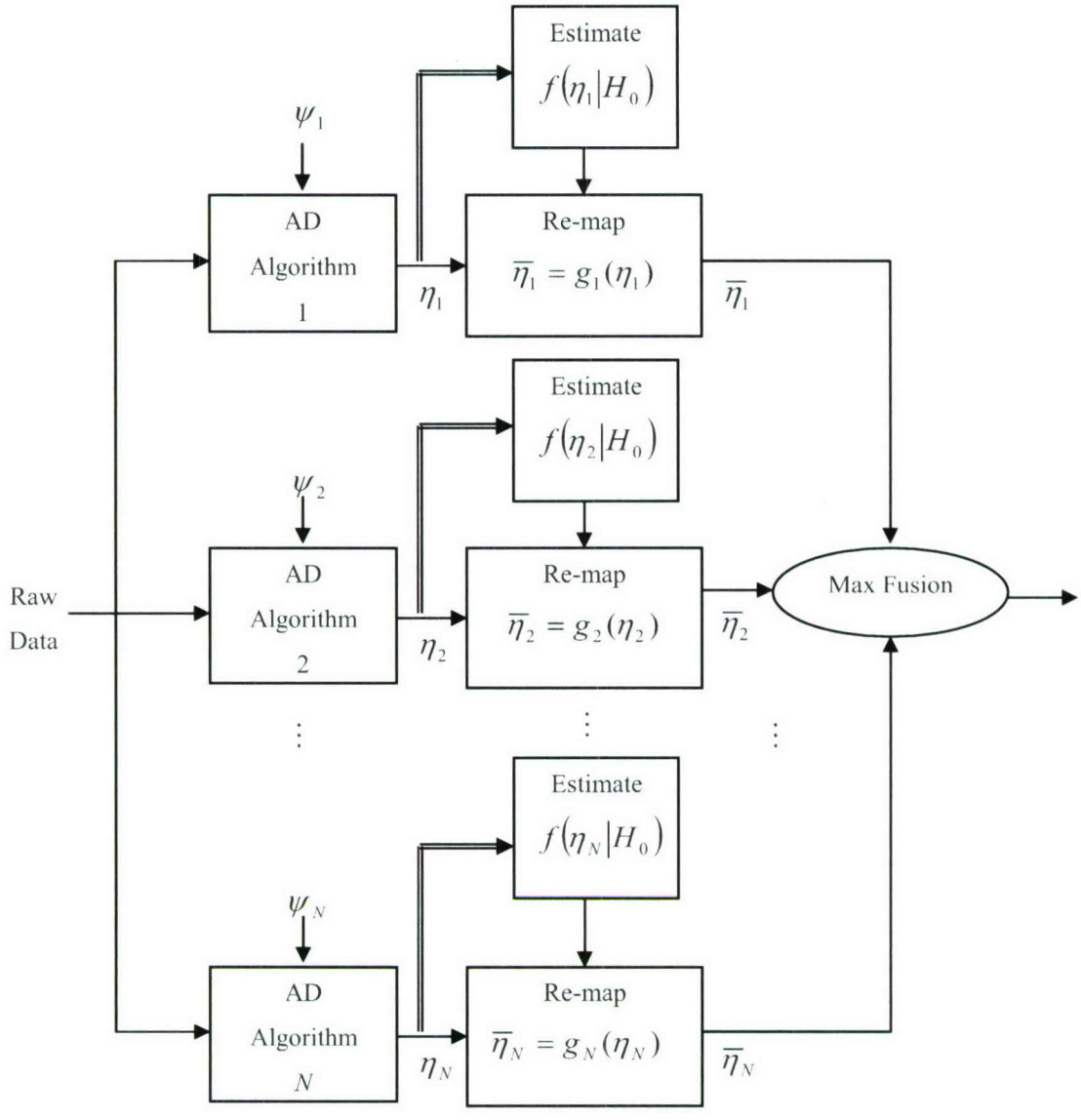

Figure 5.1. Block Diagram of the Fusion Architecture

The raw data is processed with the help of an anomaly detector for different sets of parameters. In the architecture shown in Figure 5.1, these sets of parameters are identified as $\psi_1, \psi_2, \psi_3, ...\psi_N$. The probability density function for null hypothesis of the anomaly detector statistics for each parameter set is estimated as discussed in Section 4. After modeling, the statistics values for each parameter are remapped so that they have similar probability density functions. The remapping operation is discussed in the next

subsections. The fusion operator is applied to the statistics value after remapping. For the purpose of the current anomaly detection purpose, the maximum of the outputs is taken and is termed as *max fusion.*

5.3.1. Role of Modeling in Algorithm Fusion. The RX algorithm is CFAR (Constant False Alarm Rate) only as long as the underlying assumption of the modeling is that the background is homogeneous and that it is white Gaussian. If any of the conditions is violated, the detection algorithm becomes non CFAR. Also, the RX statistics calculated for different sets of parameters have different probability distributions. That is the reason why it is important to do the modeling across algorithms as well as across frames. A remapping similar to the one discussed in Section 4.2.3 is used. The idea here is to remap each of the algorithms to a generic density function under null hypothesis so that the expected FAR for any threshold on each of the N algorithms is the same, i.e. make the detector CFAR across different algorithms or different detection parameters for the same algorithm. Also, an on-line estimation and remapping is done using a sliding window implementation as discussed in Section 4.2.2. This ensures that the algorithm is CFAR accounting for the inhomogeneities in the run.

5.3.2. Algorithm Fusion Using 'MAX' Operator. After the mapping of targets is done as outlined in the previous chapter, the resulting sets of targets represent a common basis for comparing different anomaly detector algorithms/parameters. The next step in the whole architecture specified in Figure 5.1 is to do maximization fusion. For this, zero images of the same size of the original image are formed and the target values assigned to the corresponding points on the zero image. In order to make the target points resemble mine signature closely, each one of these values (points) can be convolved with an optimal disc of radius 'r'. A Gaussian mask is convolved with this resultant image to achieve this. The same procedure is repeated for all the algorithm target sets under consideration, and the maximum of them is taken to be the fused response image. Non-maximal suppression is carried out on this resulting image. Performance of these fused target values can be compared with the performance of individual algorithm sets. The fusion algorithm should result in a performance that equals or betters the performance of the parameter set closest to the size of the target that is being evaluated.

5.4. FUSION RESULTS FOR SIMULATED DATA

The results of algorithm fusion for simulated data is listed and explained in this section. The simulated data that is used here is generated and processed in the manner previously explained in Section 4. A Monte-Carlo [38] collection of M (= 50) images are used for processing and the results are calculated. The performance of the fusion scheme is measured with the help of Receiver Operating Characteristic (ROC) curves [45]. ROC curves display the plot of the probability of detection against the false alarms at different thresholds of the test statistic. In the case of airborne detection, a better way to plot would be the false alarms rate (FA/m^2). Semi-logarithm ROC plots for FAR vs probability of detection are generated for better representation. The results are explained in more detail in the following sub-sections for uncorrelated background data and for correlated background data with two levels of correlation. The results for real world landmine data are discussed in Section 5.6.

5.4.1. Uncorrelated Background Simulation. The images generated by the Monte Carlo simulation need to be passed through the anomaly detector stage as the fusion step requires various anomaly detector outputs as input. The anomaly detector chosen for this simulation experiment is the RX algorithm. Instead of simulating the process with the help of outputs from multiple anomaly detector algorithms, the same algorithm with different parameter sets is used. In this particular experiment, parameters of (1, 5, 10), (2, 5, 10) and (3, 5, 10) are used, where (r_T, r_B, r_D) represent (target radius, blanking radius, demeaning radius) for the RX algorithm. Uncorrelated background is simulated with the help of normally distributed noise. In terms of classification of the results, various combinations of results are generated based on the target size (large, medium, small and all targets) for a non-max block size of 8. Figure 5.2 shows the results for uncorrelated background. Figures 5.2 (a), (b), (c) and (d) give the results for simulated targets in uncorrelated background noise for large targets, medium targets, small targets and all targets, respectively. The ROC curve in Figure 5.2 (d) shows that the performance of the fusion algorithm surpasses that of the individual radii when all sizes of targets are being searched. This can be attributed to the fact that targets of each type are all compared together and so fusion tends to be the best performer as it is not based

on any one particular size. Figures 5.2 (a), (b) and (c) show that the performance of the fusion algorithm is closest to the best performing target radius for each type of mine.

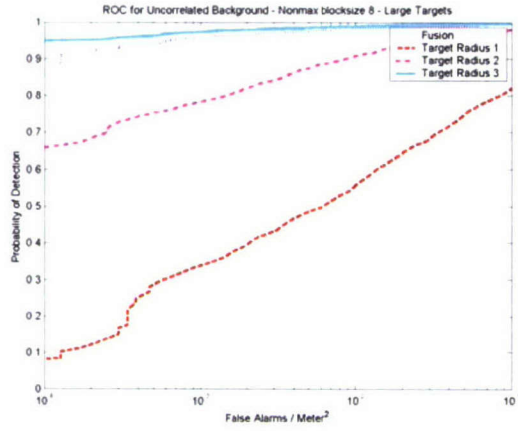

(a) Large Targets

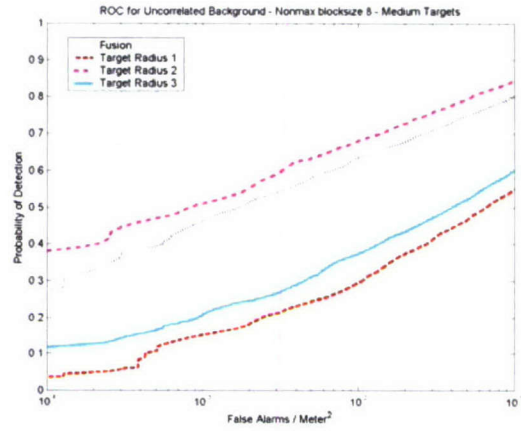

(b) Medium Targets

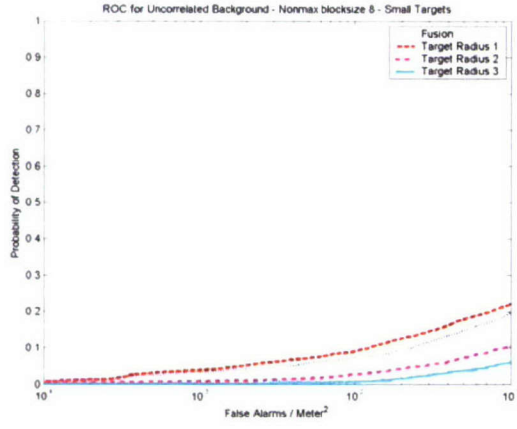

(c) Small Targets

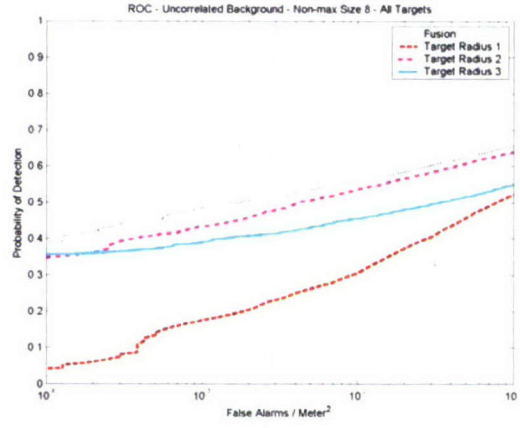

(d) All Targets

Figure 5.2. ROC Curves – Uncorrelated Noise.

5.4.2. Correlated Background Simulation. The simulated images are generated with correlated noise background as explained in Section 4.3.2. Two correlation lengths of 0.4 and 0.6 are considered and the images are generated by adding this noise. The inclusion of correlation in the background noise decreases the performance of the detection algorithm to some extent, but the performance of algorithm fusion is consistent.

The ROC curves in Figures 5.3 and 5.4 show the performance of the fusion algorithm for simulated images with correlated background noise. Figures 5.3 (a), (b), (c) and (d) show the performance for a correlation length of 0.4 and Figures 5.4 (a), (b),

(c) and (d) show the performance for a correlation length of 0.6, for large targets, medium targets, small targets and all targets, respectively. As expected the performance of the fusion algorithm is closest to the target size that is the best match for the size of the target being evaluated and surpasses all other target performances when all sizes of targets are evaluated. This illustrates that algorithm fusion described here, can be used for any target size and can be expected to perform quite well. The generalization need not stop with target size, as this is a parameter that is typical to the RX anomaly detector algorithm. In general, the algorithm fusion of different algorithms in a similar fashion is possible. Detection fusion for imagery from different sensors may also be possible if adequate registration between the imagery from different sensors is available.

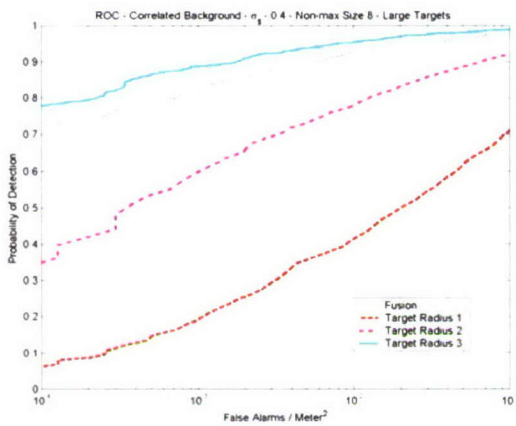

(a) Large Targets

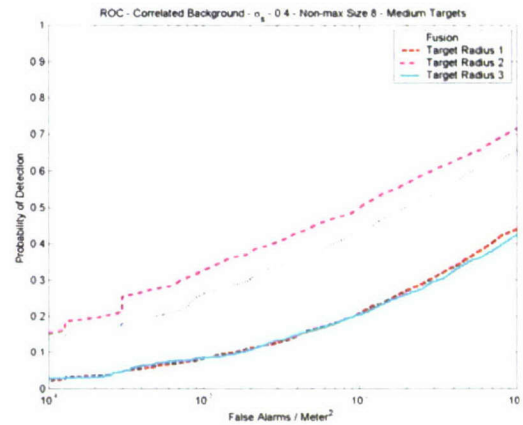

(b) Medium Targets

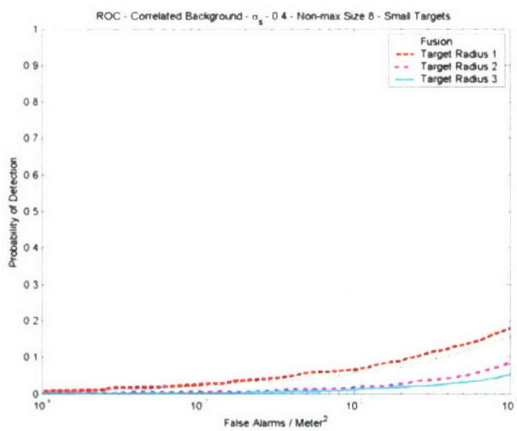

(c) Small Targets

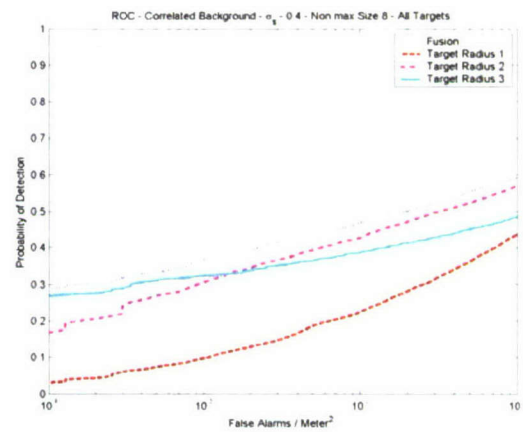

(d) All Targets

Figure 5.3. ROC Curves – Correlated Noise – Length – 0.4.

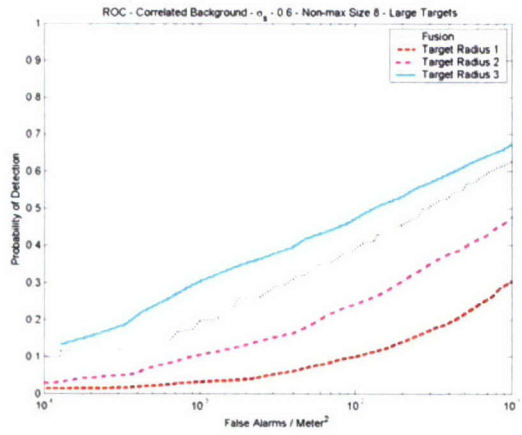

(a) Large Targets

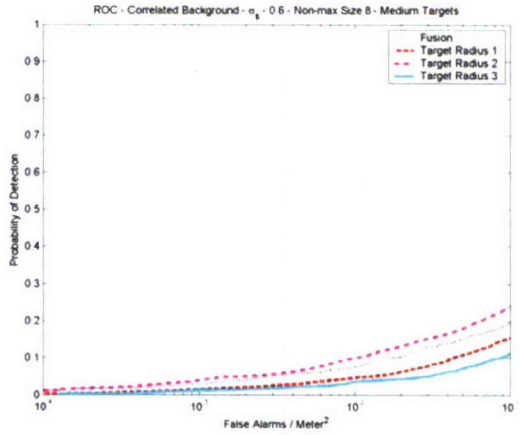

(b) Medium Targets

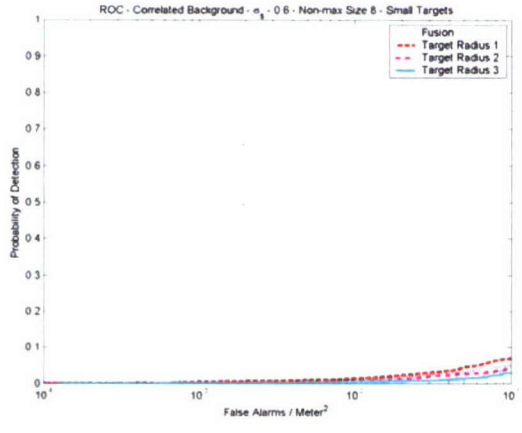

(c) Small Targets

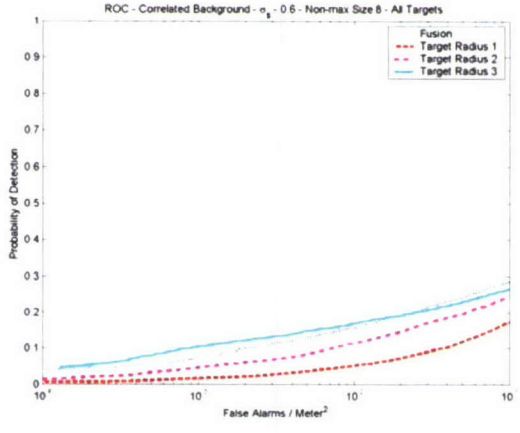

(d) All Targets

Figure 5.4. ROC Curves – Correlated Noise – Length – 0.6.

It is to be noted that the fusion scheme here is limited to MAX operation between different results in order to help improve the probability of detection. However, other fusion schemes can also be easily evaluated since detections have been remapped as discussed earlier.

6. CONCLUSION AND FUTURE WORK

The preliminary data analysis was done on almost the entire collection of data. This analysis presented a very good insight to the characteristic features of the data like the mean contrast and the standard deviation. The box plots gave a decisive comparison between the signatures of various surface mines present in the data along with statistics for false alarms.

The modeling of the background terrain yielded very good results and can be used as a highly effective tool in characterizing the background. The simulated data demonstrated the ability of background modeling to perform very well for real world like situations. For the simulated data, highly accurate models were obtained for both uncorrelated and correlated background. The effectiveness of the model in characterizing the anomaly detector output using a constant false alarm rate was demonstrated for a variety of background terrain.

Algorithm fusion was developed as a tool to optimize the anomaly detector performance. With a given set of input algorithms, the algorithm fusion scheme was able to perform close to the best performing algorithm in most cases and even surpass all of them in some cases of simulated data.

In the future, a better scheme for the parameter estimation for the model can be devised. The prediction-error method proved to be computationally expensive when the number of parameters to estimate is high along with an increase in the sample space for each parameter. A better way to do parameter estimation would be to adopt the Expectation-Maximization [46] approach to parameter estimation. Better models can also be devised with the help of Gaussian and other mixture models. Statistics for non-null hypothesis will facilitate the estimation of detection results in terms of the ROC curves. Other methods of algorithm fusion utilizing operators like AND, etc. can be tried for less separable algorithm performance.

APPENDIX A
THE LAMDFAM GUI

A.1. THE LAMDFAM GUI – PURPOSE

A Graphical User Interface (GUI) is a highly visual and user-friendly way of processing "hard to see" algorithms and procedures. The primary motivation for the development of the LAMDFAM GUI [37] is to facilitate the analysis of mine detection performance for airborne imagery collected as part of the ongoing mine detection program. In addition to allowing an easy interface to process airborne imagery, the current GUI (LAMDFAM GUI version 1.0) also facilitates comparative evaluation of different anomaly detection and false alarm mitigation algorithms. The GUI also allows users to evaluate performance using different choice of thresholding schemes at the anomaly detection and false alarm mitigation stages of the minefield detection process. The GUI has been developed using MATLAB 6.5 R13 platform utilizing the GUIDE Layout tool and appropriate background programming. The front end view of the LAMDFAM GUI looks as shown in Figure A.1.

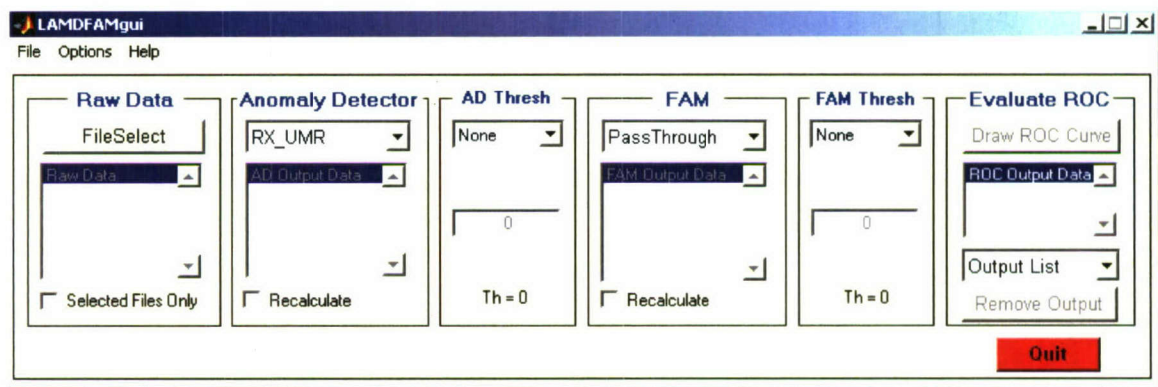

Figure A.1. Front End View of the LAMDFAM GUI

A.2. ROLE IN THE THESIS

The LAMDFAM GUI can prove to be a very useful tool for measuring the performance of the algorithm fusion procedure which is one of the primary topics of this thesis. In the case of algorithm fusion discussed in Chapter 5, the target lists that have been remapped according to a monotonic function are saved in separate directories. The fused output target list is also saved in its own directory. If these directories are considered as special anomaly detector outputs, the ROC curves for each of these target lists can be evaluated and compared with each other and all the individual algorithm /

parameter target lists can be compared to the fused output. The advantage of using the LAMDFAM GUI for this purpose is that, the algorithms can be quickly and efficiently compared.

Apart from the algorithm fusion procedure, the LAMDFAM GUI is a great tool to compute the anomaly detector response which is integral to the processing done in this thesis. Since the anomaly detector responses are needed throughout the work done, the computation of this statistic can be done across multiple sets of data in bulk such that the required anomaly detector statistics are available for modeling and processes there on.

A.3. LAYOUT AND ORGANIZATION OF THE GUI

The layout of the LAMDFAM GUI has been designed keeping the actual flow of the overall process in mind. Consequently, it has four primary modules, the Raw Data Selection Module, the Anomaly Detection Module, the False Alarm Mitigation Module and the ROC & Analysis Module. Only a preliminary introduction to the LAMDFAM GUI has been presented in this appendix. A detailed description of each of the blocks of the GUI and the functionality is discussed in [37].

The raw data module on the GUI helps selection of the list of frames to process. The selected frames are listed in the raw data list box. Raw imagery data for any frame can be displayed by double-clicking the name of the frame in the list box. The raw images are processed by the anomaly detection module.

The anomaly detection (AD) module on the GUI basically runs the anomaly detection algorithm that is chosen from the popup menu in AD block. The AD threshold block allows the user to choose among various schemes for thresholding of the target list generated by the anomaly detector. Double clicking the name of any frame in the list box in AD block displays the anomaly detection output. If AD thresholding has been specified, it also shows the detected targets by marking a square box at each target locations.

The false alarm mitigation (FAM) module on the GUI runs a particular false alarm mitigation algorithm that is selected from the popup menu in FAM block. The FAM threshold block allows the user to choose among various schemes for thresholding of the target list generated by the false alarm mitigation algorithm. Double clicking the

name of any frame in the list box in FAM block displays the raw image along with the detections from the FAM block as per the selected FAM thresholding scheme.

The ROC & analysis module of the GUI displays ROC curves for the mine detection schemes and also allows the user to analyze and compare the performance of different algorithms. Double clicking on any entry in the list box in the ROC block displays the raw image and the detections for each of the algorithms, thus allowing the user to compare the performance of various algorithms for any specified frame.

APPENDIX B
FUNCTION REFERENCE

B.1. Function Name : clutterModelfor3paramBeta

Description

Primary function which performs the modeling of the background, by the prediction – error method. It computes the best fit parameters and returns the best fitting distribution values.

Usage

[*testdist,bestalpha,bestbeta,bestN,bestlambda,xCvals,hCvals*]
= clutterModelfor3paramBeta(*Cluttervals*)

Inputs

Cluttervals – set of RX response values reprensenting the background

Outputs

testdist – the modeled distribution after estimation of parameters

bestalpha – best value for the γ parameter of the generalized beta distribution

bestbeta – best value for the η parameter

bestN – best value for the parameter N as shown in section 3.5

bestlambda – best value for the parameter λ

xCvals – the transformed RX statistic ranging from 0.5 to 1

hCvals – the observed distribution before estimation of parameters

B.2. Function Name : doFusion

Description

The main function which computes the algorithm fusion over different parameters of the RX algorithm with the help of the 'MAX' operator.

Usage

done = doFusion(*dynamic_List, newNonmaxDir, finNonmaxDir, sizImg*)

Inputs

dynamic_List – input list of filenames to be fused

newNonmaxDir – the directory / folder (s) where the mapped values for fusion are stored

finNonmaxDir – the directory / folder where the fused values are stored for each file

sizImg – size of the input image

Outputs

done – output flag that signals completion of fusion process

B.3. Function Name : mapUsingBeta

Description

Maps the input cumulative distribution function (CDF) to the basis of a standard cumulative distribution function defined.

Usage

newx = mapUsingBeta(*bestalpha, bestbeta, bestlambda*)

Inputs

bestalpha – best value of parameter γ of desired CDF

bestbeta – best value of parameter η of desired CDF

bestlambda – best value of parameter λ of desired CDF

Outputs

newx – new mapped values of the RX statistic

B.4. Function Name : compute3betaCDF

Description

Calculates the cumulative distribution function (CDF) based on the 3-parameter beta density function for the input RX statistic.

Usage

resCDF = compute3betaCDF(*xVals, bestbeta, bestalpha, bestlambda*)

Inputs

xVals – the RX statistic values for which CDF is to be computed

bestbeta – best value of parameter η of desired CDF

bestalpha – best value of parameter γ of desired CDF

bestlambda – best value of parameter λ of desired CDF

Outputs

resCDF – the resulting 3 parameter beta CDF

B.5. Function Name : formRXmapTables

Description

Forms the mapping tables of one input CDF onto the basis of another input CDF according to the input RX statistic values.

Usage

[*table_vals, table_indices*] = formRXmapTables(*CDFvalstoMap, refCDFvals, refxVals*)

Inputs

CDFvalstoMap – the CDF values which need to be mapped onto a standard CDF

refCDFvals – the reference CDF values to which the new CDF values are to be mapped

refxVals – the reference RX statistic values which forms the common basis

Outputs

table_vals – the mapped values from one CDF to another

table_indices – the indices of the mapped values demonstrating the mapping

B.6. Function Name : mapnewRXtotargetsV2

Description

Performs the actual mapping of the new RX statistic values from the mapping tables to the actual targetlists.

Usage

[*done, new_targets*] = mapnewRXtotargetsV2(*NonmaxDir, list_file, trans_xVals*)

Inputs

NonmaxDir – directory / folder where the original RX values are stored

list_file – the list of files to be mapped

trans_xVals – the mapped values

Outputs

done – confirmation flag for completion of the mapping process

new_targets – the new targetlist that has been formed by the mapping (to be saved)

B.7. Function Name : formClutterfor4params

Description

Forms the list of clutter values from a list of files. Treats all detection points as clutter

Usage

[*Cluttervals*] = formClutterfor4params(*NonmaxDir, listoffiles*)

Inputs

NonmaxDir – directory / folder where the targetlist is stored

listoffiles – list of files (frames) to be considered

Outputs

Cluttervals – list of clutter that has been formed from the files

B.8. Function Name : computeModelnSave

Description

Wrapper function for computing the background model, doing the mapping of values and saving the mapped values.

Usage

[*bestalpha, bestbeta, bestlambda, bestN*]

= computeModelnSave(*computeFusion, lin_idx, listoffiles, NonmaxDir, newNonmaxDir, validateFlag, varargin*)

Inputs

computeFusion – flag to turn the fusion process on or off

lin_idx – index variable maintained for plotting models

listoffiles – list of files to be processed

NonmaxDir – directory / folder where targetlist files are present

newNonmaxDir – directory / folder where the mapped values are to be saved

validateFlag – flag that says whether the data is simulated or real world data

varargin – multiple input arguments based on whether the process is for simulation or not and whether the sliding window implementation is being done or not

Outputs

bestalpha – best value of parameter γ

bestbeta – best value of parameter η

bestlambda – best value of parameter λ

bestN – best value of parameter N

B.9. Function Name : MineStats_new

Description

Function to calculate the preliminary mine statistics reported in section 2.6.

Usage

[*meanoMines*] = MineStats_new(*dataStr, band, area, mission, dnflag*)

Inputs

dataStr – string which specifies the particular data collection used

band – string that specifies the band for which the statistics have to be computed

area – string that specifies the area for which the statistics have to be computed

mission – string that specifies the mission for which the statistics have to be computed

dnflag – flag that switches between daytime and nighttime images

Outputs

meanoMines – the output structure that contains all the statistics required

B.10 Function Name : getListofFiles

Description

Gets the runs required for a specific set of input filters

Usage

[*runs_needed*] = getListofFiles(*dataDir, datasets, band, area, mission, rmines, truthList, dnflag*)

Inputs

dataDir – directory / folder that contains the required data

datasets – set of datasets to filter from

band – string that specifies the required band

area – string that specifies the required area

mission – string that specifies the required mission

rmines – set of mines to be rejected – this is useful for the selection of files

truthList – a comprehensive structure that contains the truth data

dnflag – flag that switches daytime and nighttime images

Outputs

runs_needed – the filtered runs required for processing

BIBLIOGRAPHY

1. C. L. Brown, and A. M. Zoubir, "Landmine Detection using Single Sensor Metal Detectors," *Proceedings of the IEEE, International Conference on Acoustics, Speech and Signal Processing*, Vol. 4, pp. IV - 3948 – IV - 3951, May 2002.

2. S. L. Earp, and E. S. Hughes, "Ultra-Wideband Ground-Penetrating Radar for the Detection of Buried Metallic Mines," *Proceedings of the IEEE, National Radar Conference*, pp. 7 – 12, May 1996.

3. I. J. Won, and H. Huang, "Detection and Identification of Landmines using Electromagnetic Induction Spectroscopy," *IEEE International Remote Sensing and GeoScience Symposium, IGARSS '02*, Vol. 3, pp. 1553 – 1555, June 2002.

4. C. P. Datema, V. R. Bom, and C.W. E. van Eijk, "Landmine Detection with the Neutron Backscattering Method," *IEEE Transactions on Nuclear Science*, Vol. 48, No. 4, pp. 1087 – 1091, August 2001.

5. Y. Tan, S. L. Tantum, and L. M. Collins, "Landmine detection with Nuclear Quadrupole Resonance," *IEEE International Remote Sensing and GeoScience Symposium, IGARSS '02*, Vol. 3, pp. 1575 – 1578, June 2002.

6. R. Denier, and T. J. Herrick, "Vibration Analysis of Landmine Detection using High-Pressure Waterjets," *Proceedings of the SPIE*, Vol. 4038, No.2, pp. 1364 – 1371, 2000.

7. M. V. Kumar, and F. Sahin, "A Swarm Intelligence based Approach to the Mine Detection Problem," *IEEE International Conference on Systems, Man and Cybernetics*, Vol. 3, pp. 6, October 2002.

8. Y. Zhang, M. Schervish, and H. Choset, "Probabilistic Hierarchial Spatial Model for Mine Locations and its Application in Robotic Landmine Search," *Proceedings of the IEEE, International Conference on Intelligent Robots and Systems*, pp. 681 – 689, October 2002.

9. D. R. Brown, "Multisensor Vehicular Mine Detection Testbed for Humanitarian Demining," *Proceedings of the Technology and the Mine Problem Symposium*, Monterey, CA: Naval Postgraduate School, pp. 4-73/4-78, 1996.

10. Time Magazine, *Best Inventions of 2002 – Landmine Destroyer ELADIN,* November 2002.

11. R. Siegel, "Landmine Detection," *IEEE Instrumentation and Measurement Magazine*, Vol. 5, Issue 4, pp. 2805 – 2809, December 2002.

12. R. Rupp, "LAMD – Program Overview," *NDIA symposium*, October 2000.

13. J. Gasson, and D. Hughes, "Development of an Ultra-Wideband SAR for Minefield Detection," *Proceedings of the IEEE, International Geoscience and Remote Sensing symposium, IGARSS '99*, Vol. 5, pp. 2474 – 2476, July 1999.

14. H. T. Haskett, and D. A. Reago, "Identification of Optimal Bands in the 3-5 um Region for Lightweight Airborne Mine Detection System(LAMD)," *SPIE- Detection and Remediation of Mine and Minelike Targets VI*, Vol. 4394, pp. 246-257, 2001.

15. S. F. Thornton, and J. M. F. Moura, "The Fully Adaptive GMRF Anomaly Detector for Hyperspectral Imagery," *Proceedings of the IEEE, International Conference on Acoustics, Speech and Signal Processing, ICASSP '00*, Vol. 1, pp 37 – 40, June 2000.

16. N. H. Witherspoon, J. H. Holloway Jr., K. S. Davis, R.W. Miller, and A. C. Dubey, "The Coastal Battlefield Reconnaissance and Analysis (COBRA) Program for Minefield Detection," *Proceedings, SPIE- Detection Technologies for Mines and Minelike Targets*, Vol. 2496, pp. 500-508, 1995.

17. G. Maksymonko, and K. Breiter, "ASTAMIDS Minefield Detection Performance at Aberdeen Proving Ground Test Site," *Proceedings of SPIE*, Vol. 3079, pp. 726-737, 1997.

18. ESTCP Cost and Performance Report, "Assessment of the Remote Minefield Detection System (REMIDS)," U.S. Department of Defense, September 1999.

19. H. H. Suzukawa, Jr, and M. S. Farber, "Long-Range Airborne Detection of Small Floating Objects," *Proceedings of the SPIE, Detection Technologies for Mines and Minelike Targets*, Vol. 2496, pp. 193-205, 1995.

20. J. R. Simrad, and P. Mathieu, "Airborne Far IR Minefield Imaging System(AFIRMIS): Description and Preliminary Results," *Proceedings of the SPIE, Detection and Remediation of Mine and Minelike Targets III*, Vol. 3392, pp. 84-95, 1998.

21. Q.A. Holmes, "Adaptive Multispectral CFAR Detection of Landmines," *Proceedings of the SPIE, Detection Technologies for Mines and Minelike Targets*, Vol. 2496, pp. 421 – 432, 1995.

22. I. S. Reed, and X. Yu, "Adaptive Multiple-Band CFAR Detection of an Optical Pattern with Unknown Spectral Distribution," *IEEE Transactions on Acoustics, Speech and Signal Processing*, Vol. 38, No. 10, pp. 1760 – 1770, October 1990.

23. P. Sriram, "False Alarm Mitigation using Grayscale Moment Invariants for Airborne Mine Detection," Masters' Thesis, University of Missouri Rolla, 2003.

24. S. Kummamuru, "Spatial Point Processes for Airborne Minefield Detection," Masters' Thesis, University of Missouri Rolla, 2002.

25. S. Agarwal, and H. Ramachandran, "Algorithms and Architecture for Airborne Minefield Detection," *Proceedings, SPIE – Detection and Remediation of Mine and Minelike Targets VII*, Vol. 4742, pp. 96 – 107, 2002.

26. B. A. Baertlein, W. J. Liao, and I. K. Sendur, "Modeling and Signal Processing Support to the Light Airborne Multispectral Minefield Detection (LAMD-I) Program," *Final Report*, November 2001.

27. X. Yu, and I.S. Reed, "A Robust Adaptive Multispectral Object Detection by Using the Wavelet Transform," *Proceedings of the IEEE, International Conference on Acoustics, Speech and Signal Processing, ICASSP '92*, Vol. 5, pp. 141 – 144, March 1992.

28. D. W. J. Stein, "Modeling Variability in Hyperspectral imagery using a Stochastic Compositional Approach," *International Geoscience and Remote Sensing Symposium, IGARSS '2001*, Vol. 5, pp. 2379 – 2381, July 2001.

29. C. H. Fosgate, and H. Krim, "Multiscale Segmentation and Anomaly Enhancement of SAR Imagery," *IEEE Transactions on Image Processing*, Vol. 6, No.1, pp. 7 – 20, January 1997.

30. S. G. Beaven, and D. W. J. Stein, "Comparison of Gaussian Mixture and Linear Mixture Models for Classification of Hyperspectral Data," *International Geoscience and Remote Sensing Symposium, IGARSS '2000*, Vol. 4, pp. 1597 – 1599, July 2000.

31. S. Zhang, and J. Jin, "Computation of Special Functions," *Wiley & Sons*, New York, 1996.

32. R.J. Adler, "The Geometry of Random Fields," *Wiley & Sons*, New York, 1981.

33. C. I. Chang, and S. S. Chiang, "Anomaly Detection and Classification for Hyperspectral Imagery," *IEEE Transactions on Geoscience and Remote Sensing*, Vol. 40, No.6, pp. 1314 – 1325, June 2002.

34. T. P. Gia, and Q. P. Duong, "The Generalized Beta and F- Distributions in Statistical Modeling," *Mathematical and Computer Modeling*, Vol. 16, pp. 1613 – 1625, 1989.

35. N. L. Johnson, S. Kotz, and N. Balakrishnan, "Continuous Univariate Distributions – Volume 2," *Second Edition, Wiley & Sons*, New York, 1995.

36. E. Weyer, R. C. Williamson, and I. M. Y. Mareels, "Finite Sample Properties of Linear Model Identification," *IEEE Transactions on Automatic Control*, Vol. 44, No. 7, pp. 1370 – 1383, July 1999.

37. H. Ramachandran, and S. Agarwal, "LAMDFAM : GUI for the Evaluation of Mine Detection Algorithms – User Manual (draft)," 2003.

38. M. Ivanovic, and D. A. Weber, "Monte-Carlo Simulation Study of Multi-window Imaging," *IEEE Nuclear Science Symposium and Medical Imaging Conference*, Vol. 3, pp. 1301 – 1304, Nov. 1994.

39. S. Agarwal, and H. Ramachandran, "LAMD 2003 WESCAM Data processing (Mine Detection Performance) – Report," *NVESD Countermine Division*, January 2003.

40. H. Ren, and J. Jian, "A Preliminary Research into the Data Fusion of the Double Homing Head," *Proceedings of the IEEE, International Conference on Signal Processing*, pp. 1803 – 1806, 2002.

41. G. J. Dobeck, "Algorithm Fusion for Automated Sea Mine Detection and Classification," *OCEANS 2001. MTS/IEEE Conference and Exhibition*, Vol. 1,pp 130 – 134, November 2001.

42. D. Casasent, and A. Ye, "Detection Filters and Algorithm Fusion for ATR," *IEEE Transactions on Image Processing*, Vol. 6, No.1 pp. 114 – 125, January 1997.

43. T. Aridridges, M. Fernandez, and G. J. Dobect, "Fusion of Adaptive Algorithms for the Classification of Sea Mines using High Resolution Side-scan SONAR in very Shallow Water," *OCEANS 2001. MTS/IEEE Conference and Exhibition*, Vol. 1, pp 135 – 142, November 2001.

44. H. R. Tizhoosh, "Observer Dependent Image Enhancement," *10th IEEE Conference on Fuzzy systems*, Vol. 1, pp. 23 – 26, December 2001.

45. W. W. Peterson, T. Birdsall, and W. Fox, "The Theory of Signal Detectability," *IEEE Transactions on Information Theory*, Vol. 4, No. 4, pp. 171 – 212, September 1954.

46. G. J. McLachlan, and T. Krishnan, "The EM Algorithm and Extensions," *Wiley Series in Probability and Statistics*, Wiley and Sons, 1997.

47. K. V. Mardia, J. T. Kent, and J. M. Bibby, "Multivariate Analysis," *Academic Press Inc*, 1979.

VITA

Hariharan Ramachandran was born on October 2, 1979 in Salem, India. In May 2001, he received his Bachelor of Engineering Degree in Electronics and Communication Engineering from Bharathiar University, India. He joined the Master of Science program in Electrical Engineering at the University of Missouri – Rolla in Fall 2001. While pursuing his graduate degree, he was supported by the Department of Electrical Engineering as a Graduate Research Assistant. He received his Master of Science Degree in Electrical Engineering from the University of Missouri – Rolla in May 2004.

Distribution List

8 Director
Night Vision And Electronic Sensors Directorate
10221 Burbeck Road
Attn: AMSRD-CER-NV-CMD
Fort Belvoir, VA 22060-5806

2 Defense Technical Information Center
8725 John J. Kingman Highway
Suite 0944
Fort Belvoir, VA 22060-6218